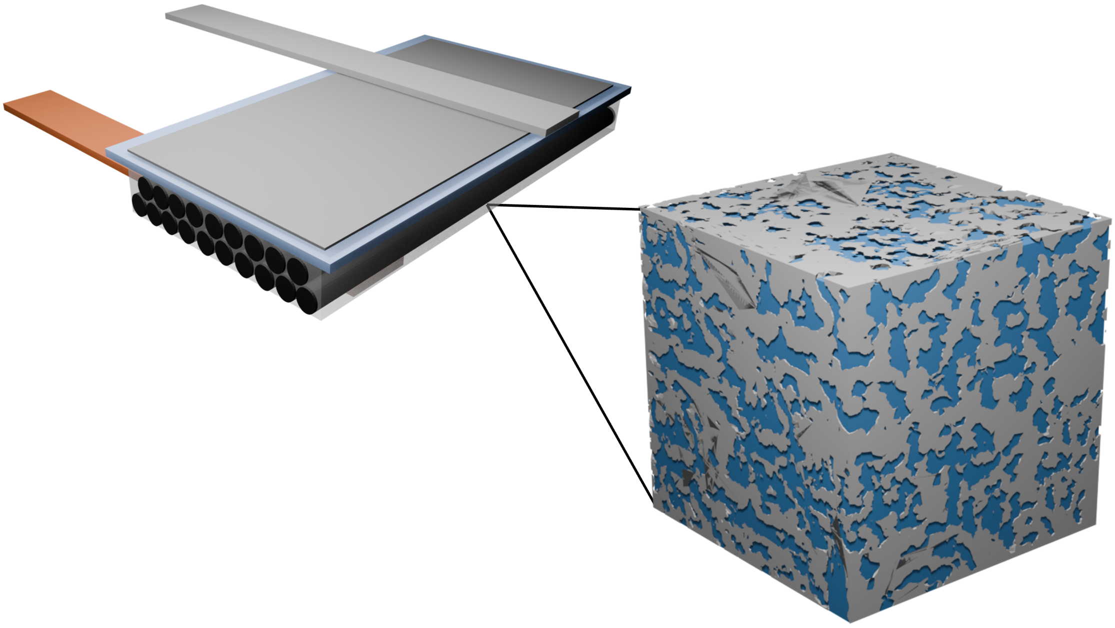

Towards low-temperature structural battery electrolytes for sustainable multifunctional energy storage

Master's thesis in Materials Chemistry

Elin Lager

DEPARTMENT OF INDUSTRIAL AND MATERIALS SCIENCE

CHALMERS UNIVERSITY OF TECHNOLOGY
Gothenburg, Sweden 2026
www.chalmers.se

Master's thesis 2026

Towards low-temperature structural battery electrolytes for sustainable multifunctional energy storage

Elin Lager

Department of Industrial and Materials Science
Chalmers University of Technology
Gothenburg, Sweden 2026

Towards low-temperature structural battery electrolytes for sustainable multifunctional energy storage

ELIN LAGER

Supervisor: Johanna Xu, Department of Industrial and Materials Science
Examiner: Anna Martinelli, Department of Chemistry and Chemical Engineering

Master's Thesis 2026
Department of Industrial and Materials Science
Chalmers University of Technology
SE-412 96 Gothenburg
Telephone +46 31 772 1000

Cover: A schematic of a structural battery half-cell with a zoomed in schematic of the structural battery electrolyte for low temperature application.

Typeset in LaTeX
Gothenburg, Sweden 2026

Towards low-temperature structural battery electrolytes for sustainable multifunctional energy storage

Elin Lager
Department of Industrial and Materials Science
Chalmers University of Technology

Abstract

The electrification of the transport sector has increased the demand for efficient and lightweight energy systems. One promising solution is structural batteries which are multifunctional materials that store energy and carry mechanical load, simultaneously. This multifunctionality is enabled partly by the structural battery electrolyte, a semi-solid electrolyte consisting of a liquid electrolyte for ionic transport, and a porous polymer providing mechanical stability. However, at low temperatures ($<$ -30 °C), these systems exhibit a significant loss of capacity due to increased viscosity or freezing of the electrolyte, limiting ion transport. This presents a critical challenge for applications in Nordic climates, defence, and aerospace systems, where operation is in extreme cold. In this thesis, six different techniques were used to analyse the electrochemical and mechanical performance of five novel electrolyte systems. The results found that the diglyme-based electrolytes showed improved electrochemical performance compared to the reference electrolyte, with the 70:30 DG:FEC composition exhibiting the highest ionic conductivity in the range of 10^{-4} S/cm at 25 °C and 10^{-6} S/cm at -40 °C. This system also showed a specific capacity of 430 mAh/g at 25 °C and maintained over 100 mAh/g at -15 °C. Mechanical testing confirmed that the structural integrity of the electrolyte was preserved across the temperature range and morphology analysis revealed a stable electrolyte-electrode interface after cycling, with preserved porosity. Overall, the results demonstrate that diglyme-based structural electrolytes enable improved low-temperature performance while maintaining mechanical functionality, highlighting their potential for cold-climate energy storage applications.

Keywords: structural batteries, composite materials, structural battery electrolyte, organic solvent, bicontinuous system, low-temperature applications, electrochemical characterisation.

Acknowledgements

I would like to express my gratitude to Johanna Xu for your guidance, encouragement, and support throughout this master's thesis.

I would also like to thank Chesta Chesta for the invaluable help with experimental troubleshooting and positive energy throughout the project. Special thanks to Achilleas Pipertzis for extensive support with the BDS measurements and analysis, and to Marko Bek for carrying out the DMA measurements and teaching me the procedure. I am also grateful for Emilie Seignér Bökmark for support with laboratory equipment and practical assistance.

Furthermore, I would like to thank the rest of the master's thesis workers at the Department of Industrial and Materials Science for enjoyable moments and supportive atmosphere.

Lastly, I want to thank family and friends for your continuous encouragement and support during this work.

Elin Lager, Gothenburg, June 2026

List of acronyms

Listed below are the acronyms used throughout this thesis, in alphabetical order.

AIBN	2,2'-Azobis(2-methylpropionitrile)
BPAEDMA	Bisphenol A ethyoxlate dimethacrylate
CPE	Constant phase element
CV	Cyclic Voltammetry
Diglyme	Diethylene glycol dimethyl ether
DMA	Dynamic Mechanical Analysis
DSC	Dynamic Scanning Calorimetry
EIS	Electrochemical Impedance Spectroscopy
FEC	Fluoroethylene carbonate
FT	Freezing temperature
GCD	Galvanostatic Charge-Discharge
LiBOB	Lithium bis(oxalato)borate
LiDFOB	Lithium difluoro(oxalato)borate
LiTFSI	Bis(trifluoromethane)sulfonimide lithium salt
LT	Low temperature
OCP	Open circuit potential
PEGDA	Poly(ethylene glycol) diacrylate
PIPS	polymerisation-induced phase separation
RT	Room temperature
SBE	Structural Battery Electrolyte
SEI	Solid Electrolyte Interphase
SEM	Scanning Electron Microscopy

Nomenclature

A list of indicies and variables used in this thesis.

Indices

x	A fraction between 0 and 1, representing the discharged and charged states, respectively
t	Index for time step

Variables

k	Rate constant (unit depending on order of reaction)
A	Pre-exponential factor (unit depending on order of reaction)
E_A	Activation energy ($\mathrm{J\,mol^{-1}}$)
R	Gas constant (8.3145 $\mathrm{J\,mol^{-1}\,K^{-1}}$)
T	Temperature (K)
ε	Dielectric constant
E^*	Energy barrier ($\mathrm{J\,mol^{-1}}$)
k_B	Boltzmann constant ($\mathrm{J\,K^{-1}}$)
V	Potential (V)
ω	Angular velocity ($\mathrm{rad\,s^{-1}}$)
I	Current (A)
φ	Phase shift
Z	Impedance (Ω)
Z'	Real part of impedance (Ω)
Z''	Imaginary part of impedance (Ω)
j	Imaginary unit
σ^*	Complex conductivity ($\mathrm{S\,cm^{-1}}$)
σ'	Real part of conductivity ($\mathrm{S\,cm^{-1}}$)
σ''	Imaginary part of conductivity ($\mathrm{S\,cm^{-1}}$)
Z^*	Complex impedance (Ω)
d	Electrode spacing (m)
A_el	Electrode area ($\mathrm{m^2}$)

R_s	Solution resistance (Ω)
R_ct	Charge-transfer resistance (Ω)
ϵ	Strain
σ	Stress (Pa)
E'	Storage modulus (Pa)
E''	Loss modulus (Pa)
T_g	Glass transition temperature
i_p	Peak current (A)
A_ea	Electroactive area (m^2)
D	Diffusion coefficient ($\mathrm{m}^2\,\mathrm{s}^{-1}$)
C	Concentration of active species ($\mathrm{mol\,L}^{-1}$)
v	Scan rate ($\mathrm{V\,s}^{-1}$)

Contents

List of acronyms **ix**

Nomenclature **xi**

List of figures **xv**

List of tables **xvii**

1 Introduction **1**
- 1.1 Background 1
- 1.2 Purpose 1
- 1.3 Objectives 2
- 1.4 Limitations 2

2 Theory **3**
- 2.1 Structural batteries 3
  - 2.1.1 Structural battery electrolyte 4
- 2.2 Polymerisation-induced phase separation 4
- 2.3 Polymerisation mechanism 5
- 2.4 The electrochemistry behind a battery 5
  - 2.4.1 Solid electrolyte interphase 6
- 2.5 Material selection for low-temperature electrolyte systems 6
- 2.6 Electrolyte components and their functions 8
- 2.7 Characterisation techniques 9
  - 2.7.1 Scanning electron microscopy 9
  - 2.7.2 Electrochemical impedance spectroscopy 9
  - 2.7.3 Cyclic voltammetry 11
  - 2.7.4 Galvanostatic cycling 11
  - 2.7.5 Broadband dielectric spectroscopy 11
  - 2.7.6 Dynamic mechanical analysis 12

3 Materials and methods **15**
- 3.1 Materials 15
- 3.2 Manufacturing of half-cells 15
  - 3.2.1 Preparation of structural battery electrolyte 15
  - 3.2.2 Assembly of half-cells 16
- 3.3 Characterisation of the structural battery electrolyte 17
  - 3.3.1 Morphology 17
  - 3.3.2 Mechanical properties 17
  - 3.3.3 Electrochemical properties 18
- 3.4 Characterisation of half-cells 18
  - 3.4.1 Electrochemical testing 18

4 Results and discussion **19**
4.1 Copolymer selection 19
4.2 Electrochemical performance 20
4.3 Mechanical performance 26
4.4 Interfacial compatibility 28

5 Conclusion **29**

6 Future work **31**

Bibliography **33**

A Appendix 1 **I**

List of figures

2.1 Schematic of a conventional battery (left) and a structural battery (right). 4
2.2 Schematic of a structural battery electrolyte. 4
2.3 Polymerisation scheme for an acrylate (R_1=H) and methacrylate (R_1=Me), showing initiation and propagation steps. 5
2.4 Chemical structures of monomer A: bisphenol A ethoxylate dimethacrylate (BPAEDMA) and monomer B: poly(ethylene glycol) diacrylate (PEGDA). 8
2.5 Chemical structures of components used in the liquid electrolyte a) diglyme, b) FEC, c) LiTFSI, and d) LiDFOB. 9
2.6 Schematic of a Nyquist plot showing R_s, R_ct, and the equivalent circuit model. 11
2.7 Schematic of a thermogram with the loss modulus in blue, storage modulus in red, and tan(δ) in dashed black. 13

3.1 Illustration of SBE infusion. 16
3.2 Illustration of a half-cell configuration with a negative electrode against lithium metal. 16
3.3 Procedure of preparing SBE samples for SEM imaging. 17

4.1 Loss factor as a function of temperature for SBE containing only BPAEDMA and copolymers 2:1 BPAEDMA:PEGDA and 5:1 BPAEDMA:PEGDA. 19
4.2 SEM images of SBEs showing copolymers a) 2:1, b) 5:1, and c) reference. 20
4.3 Representative cyclic voltammograms for a) 100 DG, b) 70:30 DG:FEC, c) salt mix, d) 5:1 copolymer, e) reference at scan rate 0.5 mV/s. 20
4.4 Nyquist plots with a zoomed-in view showing the variation in impedance between different cells of all compositions; a) 100 DG, b) 70:30 DG:FEC, c) salt mix, d) 5:1 copolymer, e) reference. 22
4.5 Equivalent circuit model for fitting EIS data. 22
4.6 Inverse temperature dependence of ionic conductivity for different compositions of SBE. 23
4.7 Cross-sectional SEM of different SBE compositions. 24
4.8 Specific capacity for each cycle number at 25 °C, 12 °C, and -15 °C for a) 100 DG, b) 70:30 DG:FEC, c) salt mix, d) 5:1 copolymer, and e) reference. 25
4.9 a) Storage modulus and b) the loss factor as a function of temperature for SBE samples. 27
4.10 SEM images of carbon fibre imprints after cycling at room temperature for a) 100 DG, b) 70:30 DG:FEC, c) salt mix, and d) reference. 28

A.1 Opened half-cells a) 100 DG and b) 70:30 DG:FEC. I

List of tables

3.1 Compositions of all SBEs analysed. 15

4.1 Shear storage modulus (G') and calculated storage modulus (E') for different SBE compositions at three different temperatures. 27

1

Introduction

1.1 Background

Climate change and the need to reduce greenhouse gases have intensified the global transition toward sustainable transportation systems. In recent years, the electrification of vehicles has increased significantly across sectors, including automotive, aerospace, and military. This has created an increased demand for efficient, lightweight, and reliable energy storage systems, making structural batteries an increasingly important area of research.

Structural batteries are multifunctional materials that provide both load-bearing capability and electrochemical performance. Current conventional lithium-ion battery systems are monofunctional, heavy, and take up a large volume of vehicle design space. The heavy weight of conventional battery packs reduces energy efficiency and capacity, shortening the driving range. Using structural batteries instead of conventional lithium-ion batteries could drastically reduce weight. This mass reduction would lead to increased efficiency, lower energy consumption, and reduced material use. Additionally, today's batteries exhibit poor performance at low temperatures, sub 0 °C. In these climates, the electrolyte increases in viscosity or even freezes, reducing capacity, increasing safety risks, and leading to lithium plating [1]. These limitations are critical for applications used in Nordic and cold-climate environments.

In structural batteries, carbon fibres are used both as electrodes and as structural reinforcement due to their electrical conductivity, high mechanical strength and low mass density. The carbon fibres are embedded in a structural battery electrolyte (SBE), made up of a porous polymer and a liquid electrolyte, enabling ion transport between electrodes. This solid polymer matrix is ionically conductive during mechanical loading and electrically insulating to the electrodes. Current research on structural batteries is mostly focused on room temperature [2–4], while studies on low-temperature performance remain limited. At temperatures below 0 °C, ion transport and flexibility of SBEs are significantly reduced, causing capacity loss or potential mechanical failure. Therefore, new electrolyte systems must be studied for cold-climate applications.

1.2 Purpose

The aim of this thesis is to develop and characterise electrolyte systems that can operate at temperatures down to -15 °C, while preserving electrochemical and mechanical functionality.

1.3 Objectives

This thesis aims to achieve the purpose by the objectives outlined below.

- Manufacture negative half-cells with different SBE systems using polymerisation-induced phase separation (PIPS).
- Characterise the SBE systems by examining the morphology using scanning electron microscopy and performing dynamic mechanical analysis to link structure and stiffness in mechanical analysis.
- Evaluate the ionic transport behaviour from 40 °C down to -80 °C.
- Evaluate the electrochemical performance of the electrolytes in half-cell configurations with electrochemical impedance spectroscopy and conduct galvanostatic charge-discharge cycling at 25 °C, 12 °C, and -15 °C.
- Assess the compatibility of the developed SBE system with carbon fibres, with emphasis on interfacial stability and performance of low-temperature cycling.
- To create design guidelines for manufacturing SBEs for cold climate applications.

1.4 Limitations

The scope of this thesis was limited by the prior results and the given time frame. The weight ratio of resin to electrolyte was set to 50:50 for preparing the SBE solution. This supported by results from prior results showing that this system performs well in terms of ionic conductivity and mechanical stability. This was also true for the co-polymer. For the liquid electrolyte, diethylene glycol dimethyl ether (diglyme) and fluoroethylene carbonate (FEC) were used as solvents, and bis(trifluoromethane)sulfonimide lithium salt (LiTFSI) as the salt, as established in previous studies. The total salt concentration remained constant at 1 M, including the new salt.

Only half-cells of the negative electrode were assembled to simplify the system, as this thesis is at an early stage of research. Using half-cells allowed variables to be isolated, facilitating the understanding and optimisation of individual components.

Measurements on half-cells at low temperatures were limited to galvanostatic cycling at 12 °C and -15 °C. This limitation arose because other electrochemical techniques were either not available or reliably performed at lower temperatures. Additionally, no *in situ* experiments were included in this work, as the required experimental setup was unavailable.

2

Theory

This section covers the fundamentals of structural batteries and how they differ from conventional lithium-ion batteries and delves deeper into the structural battery electrolyte. The electrochemistry of a battery is covered, followed by sections how to choose materials for low-temperature applications and the electrolyte components. Lastly, all characterisation techniques used in this thesis are outlined.

2.1 Structural batteries

The left schematic in Figure 2.1 illustrates a conventional lithium-ion battery. Compared to structural batteries, conventional batteries contain particles that give no structural feature. The electrolyte is only in liquid-phase and commonly contain solvents, salts, and additives. The anode material is usually graphite particles due to their high reversibility during lithiation and low lithium potential. The cathode materials vary, as no single material meets all requirements for a good cathode, with examples including $Li_xMn_yO_z$, $LiCoO_2$, or other lithium metal oxides. Most conventional batteries have aluminium and copper as current collectors and cover the entire surface of the electrodes [5].

Structural batteries, shown to the right in Figure 2.1, are multifunctional materials that combine load-bearing capabilities with energy storage. This multifunctionality reduces the overall system weight and increases energy density [6]. Structural batteries have a negative electrode of carbon fibres and are separated from the positive electrode by a glass fibre separator in a layered structure. The positive electrode is composed of carbon fibres coated with the electrochemically active material $LiFePO_4$. Both electrodes and the separator are embedded in SBE via PIPS [7]. The carbon fibres are being the active material, structural reinforcement, and current collector, simultaneously. The SBE transports lithium ions as an ionic conductor and transfers mechanical load between fibres and lamina [8, 9]. Together, they create a stiff battery that can store energy simultaneously.

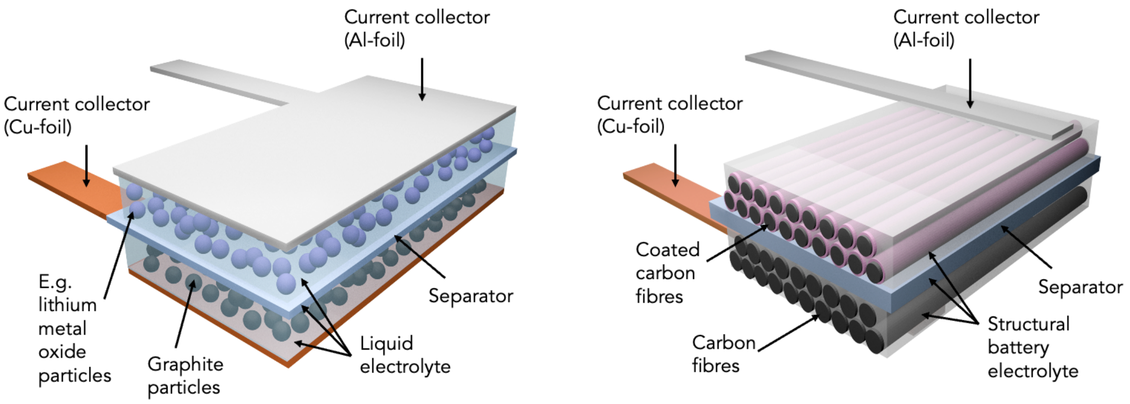

Figure 2.1: Schematic of a conventional battery (left) and a structural battery (right).

2.1.1 Structural battery electrolyte

This thesis focuses on the SBE, the semi-solid electrolyte that contributes to mechanical stiffness and ion transport. The SBE, seen in Figure 2.2, shows a porous structure of a bicontinuous system that contains a cross-linked polymer and a liquid electrolyte. The two phases have different responsibilities and contribute to the multifunctional material in different ways. The polymer provides load-transfer while the liquid electrolyte provides lithium ions that are transferred between the electrodes to charge and discharge the system [10]. The tortuosity of the structure influences ion transport, with a longer path through the porous microstructure leading to higher tortuosity. A higher tortuosity therefore results in slower ion transport between the electrodes [11]. This indicates that there is always a trade-off between ionic conductivity and mechanical performance [1].

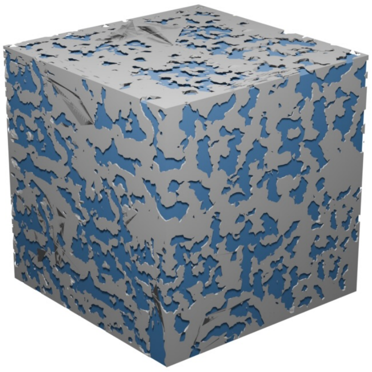

Figure 2.2: Schematic of a structural battery electrolyte.

2.2 Polymerisation-induced phase separation

PIPS is a technique used to form a bicontinuous system with a polymer-rich and solvent-rich phase in a single step. The process begins with a homogeneous mixture of solvents, monomers, and a thermal initiator. As this system cures, a 3D porous structure is formed with one phase providing stiffness and the other providing ionic conductivity. The two phases are separated by differences in the materials, such as solubility parameters, polymerization temperature, and kinetics [12, 13].

Often, phase separation is assumed to occur as polymer chains grow and become less compatible with other components. This can be the case for linear polymerisation or for step-growth cross-linking in the early stages. However, in chain-reaction cross-linking polymerisation, gelation can start before the phase separation. Gelation means that a continuous, interconnected polymer network forms in the early stages of the reaction. As gelation occurs, the polymer network is present throughout the material from the beginning. Further cross-linking reduces elasticity and forces the components to separate [13].

2.3 Polymerisation mechanism

Vinyl monomers (monomers containing -$CH{=}CH_2$) are polymerised through a free radical chain-growth mechanism, including initiation, propagation, and termination. The polymerisation mechanism affects the outcome of phase separation and is thus important, as the molecular weight increases rapidly at the beginning of chain-growth [14]. Figure 2.3 shows the initiation and propagation of the polymerisation of a methacrylate/acrylate.

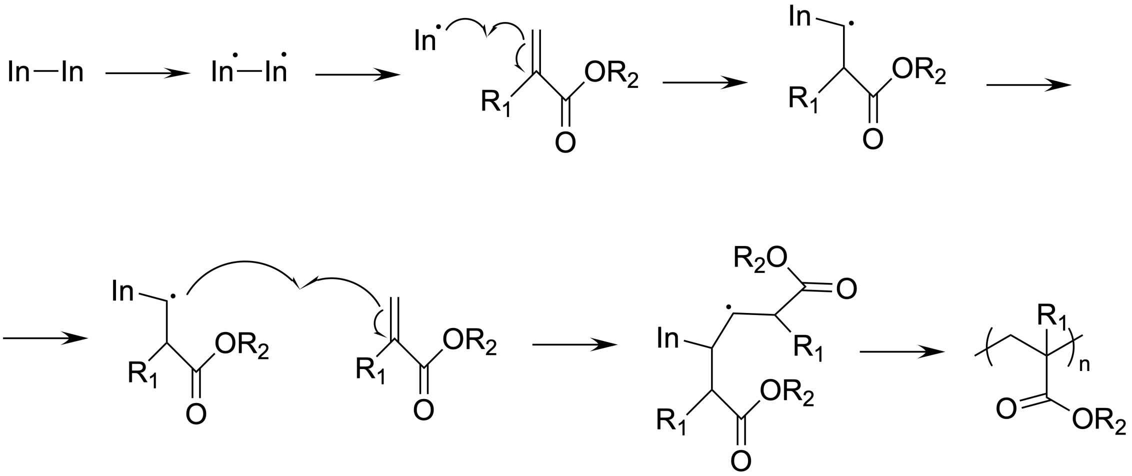

Figure 2.3: Polymerisation scheme for an acrylate (R_1=H) and methacrylate (R_1=Me), showing initiation and propagation steps.

2.4 The electrochemistry behind a battery

A rechargeable battery is an electric device that converts electrical energy to chemical energy during charging and vice versa during discharging. During charging of the battery, the cathode is oxidised (Equation 2.1), releasing electrons to move through the external circuit to the anode (Equation 2.2). Simultaneously, lithium ions are transferred from the cathode through the electrolyte and a separator membrane to the anode, where they lithiate the anode. The overall reaction is seen in Equation 2.3, where the battery is being charged in the forward reaction and discharged in the reverse reaction [15]. The transport of lithium ions occurs in several intermediate steps. The lithium ions are first deintercalated from the cathode, and solvent molecules rearrange, forming a solvation sheet around the lithium ion to stabilise the charge. The ions diffuse through the electrolyte due to concentration gradients, and the solvation sheath rearranges as they diffuse, since it is a dynamic process. Before the ions can intercalate, the anode desolvation must occur, which is a rate-limiting step that requires energy. The reverse happens during discharge [16, 17].

$$\mathrm{LiMO_2} \rightleftharpoons \mathrm{Li_{(1-x)}MO_2} + x\mathrm{Li^+} + xe^- \tag{2.1}$$

$$x\mathrm{Li^+} + xe^- + \mathrm{C_6} \rightleftharpoons \mathrm{Li}_x\mathrm{C_6} \tag{2.2}$$

$$\mathrm{LiMO_2} + \mathrm{C_6} \rightleftharpoons \mathrm{Li_{(1-x)}MO_2} + \mathrm{Li}_x\mathrm{C_6} \tag{2.3}$$

Here, Li denotes lithium ions, and x is a fraction between 0 and 1, representing fully charged or discharged states, respectively. M is a transition metal and C_6 is graphite.

2.4.1 Solid electrolyte interphase

The SEI is a thin, complex passivation layer that forms on the anode and is vital to the performance of a lithium-ion battery. The SEI forms as electrolyte components, such as solvents and salts, reduce at the anode surface. This creates a heterogeneous interphase between the metal and the electrolyte, consisting of an inner inorganic-rich layer and an outer organic-rich layer in a disordered microstructure. Inorganic compounds are relatively stable and electronically insulating, while the organic-rich layer is generally porous and accessible to the electrolyte. The SEI layer is crucial for safety, power capability, and cycle life of the battery. A key function of a stable SEI layer is to permit ions to pass through while blocking electrons from reaching the electrolyte, thereby preventing continuous electrolyte decomposition. As the battery charges and discharges, the SEI layer should remain intact, mechanically stable, and flexible. It should also have good adhesion to the anode, without delaminating [18, 19].

2.5 Material selection for low-temperature electrolyte systems

At low temperatures, batteries are subjected to several challenges, mainly due to increased viscosity, which slows ion transfer, reduces ionic conductivity, lowers capacity, worsens cyclic performance, and increases electrode resistance.

With increasing interfacial resistance, ion transport slows and solvated ions accumulate at the electrode surface, leading to sluggish ion transport kinetics. This limits the diffusion of ions in the electrode, which in turn limits the reversible capacity and rate capability. Additionally, the formation of the SEI layer is a rate-determining step at lower temperatures, as described by the Arrhenius equation (Equation 2.4), and due to the sluggish transportation, the SEI layer becomes thick and uneven [16].

$$k = Ae^{-\frac{E_A}{RT}} \tag{2.4}$$

where k is the rate constant, A the pre-exponential factor, E_A the activation energy, R the gas constant, and T the temperature in Kelvin.

The interactions between ions, solvent-ions, and solvent-solvent are increased at lower temperatures because intermolecular thermal motion is reduced, reducing the spacing between molecules [20]. A stronger ion-ion interaction can cause salting out, ion-dipole interactions make dissolution more difficult, and dipole-dipole interactions give slower kinetics. During desolvation, energy is required, and with a stronger interaction, more energy is needed, which hampers the battery's performance. The dissolvation depends on the properties of the solvation sheath which is affected by the interaction between the solvent and ion. All interactions affect the dielectric constant [20]. The dielectric constant represents polarity and measures physical and chemical properties of the solvent, such as viscosity and salt solubility. A stronger intermolecular interaction causes a higher dielectric constant. A higher dielectric constant indicates higher polarity, stronger solubility of the salt solute, and leads to salt precipitation, reducing ionic conductivity and slowing kinetics in the bulk electrolyte. The equation for the dielectric constant is shown in Equation 2.5 which shows how it is varies with temperature [16],

$$\varepsilon(T) = Ae^{\frac{E^*}{k_B T}} \tag{2.5}$$

where ε is the dielectric constant, A the pre-exponential factor, E^* the energy barrier, k_B the Boltzmann constant, and T the temperature.

To address these issues, the viscosity, freezing point, and dielectric constant must be assessed to engineer the ideal electrolyte. The interactions between the ion and the solvent should be weak to reduce the dissolution barrier, thereby accelerating the battery's reaction rate. However, a too weak interaction will slow the rate of ion transfer and enhance ion-ion interactions [16, 20]. A good cosolvent for the electrolyte is a fluorinated electrolyte with electron-withdrawing fluorine groups. This will create an inorganic, salt-rich, stable SEI layer, thereby increasing oxidative and cycling stability. An fluoroethylene carbonate (FEC) and ether-based electrolyte is ideal for low-temperature applications, as it stabilizes lithium-ion deposition, forms a SEI layer with organic substances, and increases the ion-carrier concentration, thereby enhancing lithium-ion transport [16].

The salt also plays an important role in improving performance at low temperatures. The salt affects lithium diffusion, which is linked to solubility, ionic conductivity, solvation structure, and interfacial stability. Additives such as lithium difluoro(oxalato)borate (LiDFOB) and lithium bis(oxalato)borate (LiBOB) have shown very good film-forming capability. However, they give slugging diffusion in bulk electrolyte, limited solubility, and low ionic conductivity [20].

2.6 Electrolyte components and their functions

The SBE consists of monomer(s), solvent(s), and salt(s), all with different roles. The monomers used in this thesis are represented in Figure 2.4. Bisphenol A ethoxylate dimethacrylate (BPAEDMA) is a vinyl ester monomer commonly used in crosslinked polymer systems, seen as monomer A in Figure 2.4 [21]. For a structural battery, BPAEDMA is used because of its mechanical properties and being compatible with using PIPS, enabling lithium-ion transport [1, 10].

Monomer B in Figure 2.4 illustrates poly(ethylene glycol) diacrylate (PEGDA) which was chosen to form a crosslinked copolymer with BPAEDMA. This selection was supported by a prior literature review, in which Fu *et al.* reported that the copolymer forms a thin structural battery electrolyte with satisfactory mechanical properties, high ionic conductivity, and high electrochemical stability [22]. PEGDA is a flexible monomer that increases chain mobility and free volume and is, therefore, thought to reduce the tortuosity of the SBE and enhance the ionic conductivity [23].

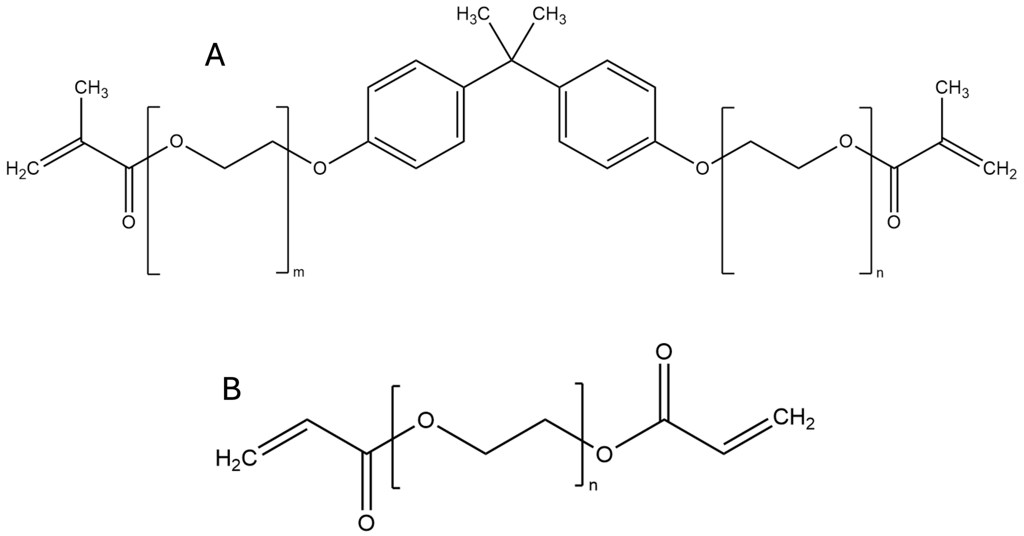

Figure 2.4: Chemical structures of monomer A: bisphenol A ethoxylate dimethacrylate (BPAEDMA) and monomer B: poly(ethylene glycol) diacrylate (PEGDA).

The liquid electrolyte consists of solvent(s) and salt(s), shown in Figure 2.5, where the salt supply lithium ions that are transported between electrodes and the solvents support ion transport [15]. Diglyme has a melting point at -64 °C making it suitable for low temperature applications [24]. It also have a low viscosity improving ion transport [25]. FEC contributes to the formation of a stable SEI layer and enhances lithium-ion transport by increasing the concentration of charge carriers. [16]. LiTFSI is a commonly used salt in batteries due to its stability over a wide temperature range, contribution to a stable SEI layer, and high solubility [26]. The additional salt, LiDFOB, is used because of its stability across a wide temperature range. The mixture of LiTFSI and LiDFOB has shown high battery performance at low temperatures in a study by Wang *et al.* [27].

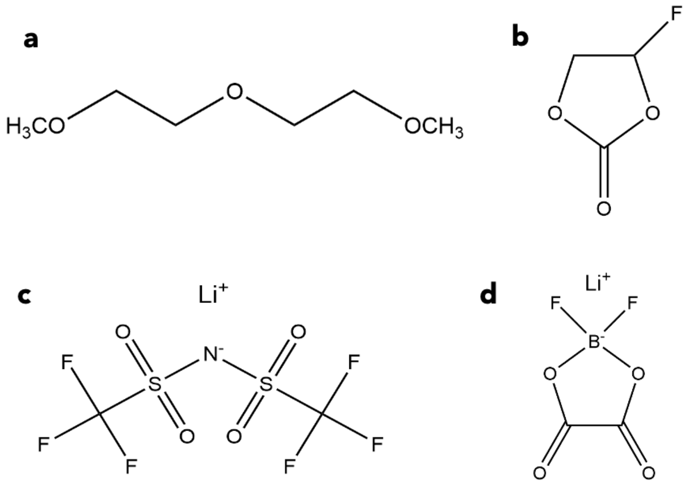

Figure 2.5: Chemical structures of components used in the liquid electrolyte a) diglyme, b) FEC, c) LiTFSI, and d) LiDFOB.

2.7 Characterisation techniques

2.7.1 Scanning electron microscopy

Scanning electron microscopy (SEM) is a microscopy technique used to characterise the morphology of specimens and can provide chemical and structural information. Electromagnetic lenses are used to focus and scan an electron beam across the surface of a sample. Several signals are produced as the electron beam interacts with the sample, with the most commonly used being secondary and backscattered electrons. Secondary electrons provide information about surface morphology, and backscattered electrons provide information about compositional density. The signals are detected by different detectors and are converted to obtain an image. The resolution of an image can be down to the nanometer scale [28].

2.7.2 Electrochemical impedance spectroscopy

Electrochemical impedance spectroscopy (EIS) is a method used to detect the resistive behaviour of an electrochemical system, by measuring the impedance. It can provide information on a wide range of processes in an electrochemical system, including the resistance of a liquid electrolyte, the charging/discharging of the electric double layer at the electrolyte/electrode interface, and the kinetics of an electrode charge-transfer reaction. Potentiostatic EIS means that the applied signal is voltage and the measured signal is current. A sinusoidal voltage signal with varying frequency is applied to a system (Equation 2.6), measuring the output current signal. The measured output signal has the same frequency as the input signal, but with a phase shift, seen in Equation 2.7,

$$V(t) = V_0 sin(\omega t) \tag{2.6}$$

$$I(t) = I_0 sin(\omega t - \varphi) \tag{2.7}$$

where V is the voltage, ω the angular velocity, t time, I the current, and φ the phase shift.

Impedance is defined as the ratio of potential to current, as seen in Equation 2.8,

$$Z(\omega) = \frac{V(\omega)}{I(\omega)} = Z' + \mathrm{j}Z'' \tag{2.8}$$

where Z' represents the real part of impedance, Z'' the imaginary part of impedance, and j is the imaginary unit.

The resulting Nyquist plot shows the real impedance against the imaginary impedance, where the lower-left-most points correspond to the highest frequencies and decrease as the points move to the right. To interpret the data, the electrochemical system must be modelled using equivalent circuit elements, such as a resistor, a capacitor, and a Warburg element. A representative Nyquist plot is seen in Figure 2.6 with a semicircle and a 45° line. This is the result of an equivalent circuit containing a resistor in series with a resistor and a capacitor in parallel, containing a Warburg element, shown in Figure 2.6. Reading the Nyquist plot reveals different elements representing different processes in the system. The solution resistance (R_s) is found at the beginning of the semicircle and refers to the resistance between the working electrode and the reference electrode. The charge transfer resistance (R_ct) represents the resistance of the ions moving across the electrolyte/electrode interface and can be found as the end of the semicircle subtracted from R_s. EIS is useful because it can detect processes occurring simultaneously but at different time scales. For example, charging of the electrochemical double layer occurs in microseconds, while diffusion occurs in hundreds of milliseconds [29, 30].

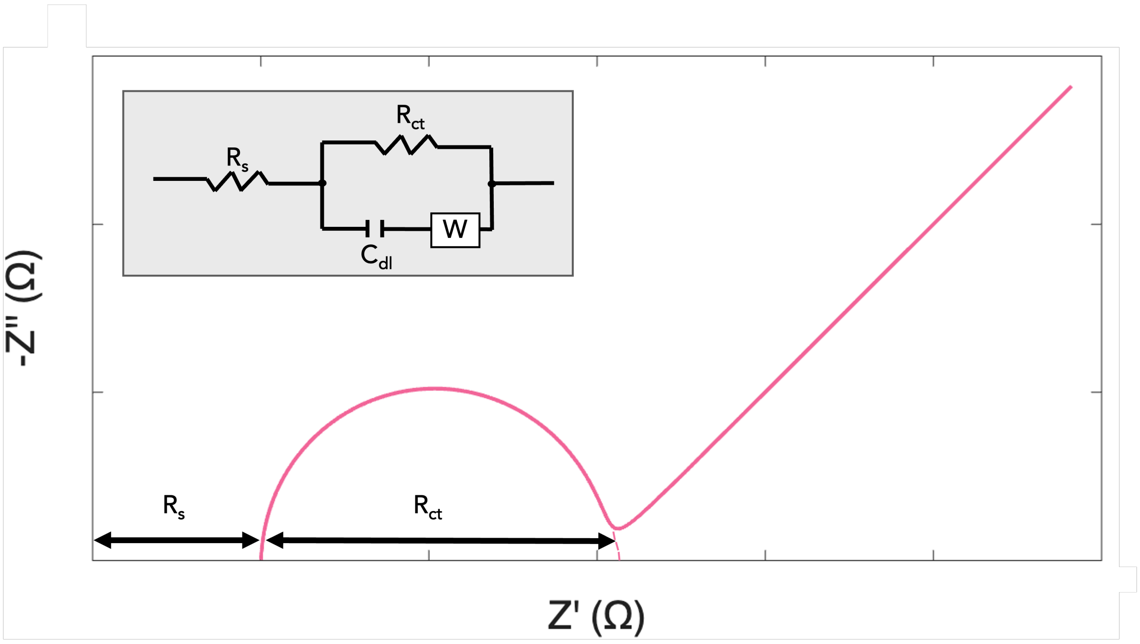

Figure 2.6: Schematic of a Nyquist plot showing R_s, R_ct, and the equivalent circuit model.

2.7.3 Cyclic voltammetry

Cyclic voltammetry (CV) is used to investigate reactions initiated by electron transfer, also referred to as redox reactions. A potential is applied to the electrochemical system in a cyclic manner, with the negative being cathodic and the positive being anodic. The resulting voltammogram shows the applied potential relative to the reference on the x-axis against the resulting current. The voltammogram shows the redox reactions of the electrochemical system as anodic (positive) and cathodic (negative) peaks. The position and height of the peaks explains the electron transfer kinetics and reaction reversibility of the system [15, 31].

2.7.4 Galvanostatic cycling

To measure the electrical performance of a battery cell, galvanostatic charge-discharge cycling (GCD) is used. A fixed current is applied at different C-rates, and the resulting voltage is measured. This measurement gives information about the cells cycle life and the specific capacity can be determined [15].

2.7.5 Broadband dielectric spectroscopy

Broadband dielectric spectroscopy (BDS) is a spectroscopic technique used to study charge transport processes and dielectric relaxation of electronic dipoles in an electric field [32]. When the sample is subjected to an alternating electric field, dipoles, ions, and atoms experience spatial displacement, resulting in a net macroscopic polarisation. An ion, a dipole, or an atom each has its own characteristic relaxation time and thus responds to the electric field with its respective resonant frequencies [33]. BDS can therefore be used to examine the ion mobility and frequency-dependent ionic conductivity behaviour of ionically conducting materials. The complex conductivity can be calculated from Equation 2.9,

$$\sigma^*(\omega) = \sigma' + j\sigma'' = \frac{1}{Z^*(\omega)}\frac{d}{A_{el}} \tag{2.9}$$

where $\sigma^*(\omega)$ is the complex conductivity, σ' the real part, σ' the imaginary part, $Z^*(\omega)$ the complex impedance, d is the electrode spacing, and A_{el} the electrode area.

2.7.6 Dynamic mechanical analysis

Dynamic mechanical analysis (DMA) is a thermal analysis technique based on rheology, the relationship between deformation and stress. The technique measures mechanical properties by applying a strain to a sample and observing the resulting stress. The sample is placed in a sample holder, where the lower end of the clamped sample is subjected to a sinusoidal strain, and the resulting stress in the fixed clamp above is measured. The applied strain is expressed by Equation 2.10 and the resulting stress by Equation 2.11. The expression for stress has a phase shift from the strain, depending on the viscoelastic response of the sample [34].

$$\epsilon(t) = \epsilon_0 sin(\omega t) \tag{2.10}$$

$$\sigma(t) = \sigma_0 sin(\omega t + \delta) \tag{2.11}$$

To separate the viscous and the elastic properties of the material, the tensile modulus, E_0, is found by division of $\sigma(t)$ and $\epsilon(t)$ and expanded using the trigonometric laws, seen in Equation 2.12.

$$\frac{\sigma(t)}{\epsilon(t)} = E_0 sin(\omega t + \delta) = E_0[sin(\omega t)cos\delta + cos(\omega t)sin\delta] \tag{2.12}$$

From this, the tensile storage modulus, E', (Equation 2.13) and the tensile loss modulus, E'', (Equation 2.14), can be obtained.

$$E' = Ecos\delta \tag{2.13}$$

$$E'' = E_0 sin\delta \tag{2.14}$$

To find the glass transition temperature (T_{g}), a temperature sweep is done, and the resulting thermogram, seen in Figure 2.7, shows the modulus against temperature. The T_{g} is determined by the maximum value of tan(δ), which is the ratio of the loss and storage modulus [34].

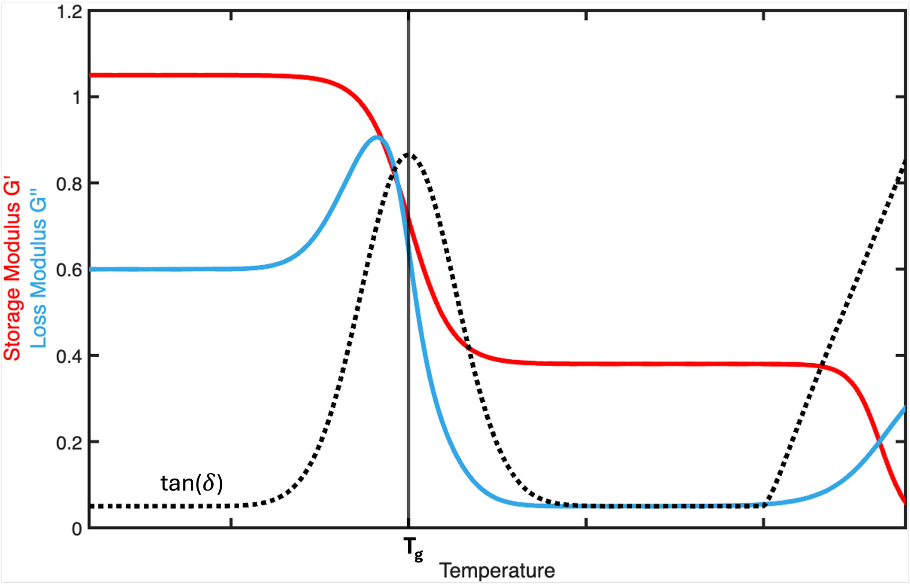

Figure 2.7: Schematic of a thermogram with the loss modulus in blue, storage modulus in red, and tan(δ) in dashed black.

3

Materials and methods

The following chapter presents the materials used in the experiments and describes the measurements performed.

3.1 Materials

For SBE manufacturing, the monomers bisphenol A ethyoxlate dimethacrylate (BPAEDMA, M_n: 540 g mol^{-1}) and poly(ethylene oxide) diacrylate (PEGDA, M_n: 700 g mol^{-1}) were used, which were procured from Sigma-Aldrich. The salts and solvents used were bis(trifluoromethane)sulfonimide lithium salt (LiTFSI), lithium difluoro(oxalato)borate (LiDFOB), diethylene glycol dimethyl ether (diglyme), fluoroethylene carbonate (FEC), and the initiator 2,2'-Azobis(2-methylpropionitrile) (AIBN), also obtained from Sigma-Aldrich. The lithium foil, nickel foil, and copper foil used in the half-cells were procured from Sigma-Aldrich. The glass microfibre filter (Whatman GF/A) was purchased from Cytvia, silver glue from Ted Pella, and carbon fibres T800S, used as electrodes, from Toray.

3.2 Manufacturing of half-cells

3.2.1 Preparation of structural battery electrolyte

Stock solutions of different liquid electrolytes were prepared in an argon atmosphere. This was done by mixing the solvent(s) with the salt until the salt was completely dissolved, using the ratios specified in Table 3.1. The SBE solution was obtained by mixing the stock solutions with the monomer(s), and 1 wt% AIBN was added with respect to the monomer. The weight ratio between the liquid electrolyte and monomer(s) was held constant at 50:50.

Table 3.1: Compositions of all SBEs analysed.

Sample name	Solvent (mass ratio)	Resin (mass ratio)	Salt (molarity)
100 DG	Diglyme	BPAEDMA	LiTFSI (1 M)
70:30 DG:FEC	Diglyme:FEC (7:3)	BPAEDMA	LiTFSI (1 M)
Salt mix	Diglyme:FEC (7:3)	BPAEDMA	LiTFSI + LiDFOB (0.8 M + 0.2 M)
2:1 copolymer	EC:PC (1:1)	BPAEDMA:PEGDA (2:1)	LiTFSI (1 M)
5:1 copolymer	EC:PC (1:1)	BPAEDMA:PEGDA (5:1)	LiTFSI (1 M)
Reference	EC:PC (1:1)	BPAEDMA	LiTFSI (1 M)

3.2.2 Assembly of half-cells

Carbon fibres were cut and glued onto a copper current collector using silver glue. Once dried, the carbon fibres were placed on a glass pane and sealed within a vacuum bag, with two tubes protruding. The vacuum bags were dried overnight and later transferred to a glovebox with an argon atmosphere. In the glovebox, the SBE solution was prepared in a syringe and attached to the vacuum bag through a tube. Both tubes were sealed with clamps, preventing any air from entering. The vacuum bag was then connected to a vacuum pump, as shown in Figure 3.1, creating a vacuum in the bag when the clamp was opened. The other clamp was then opened to allow the SBE solution to migrate over the carbon fibres in the vacuum bag. Once the SBE solution reached the opposite end, the clamps were reattached, and the vacuum bag was cured in an oven at 90 °C for 45 minutes.

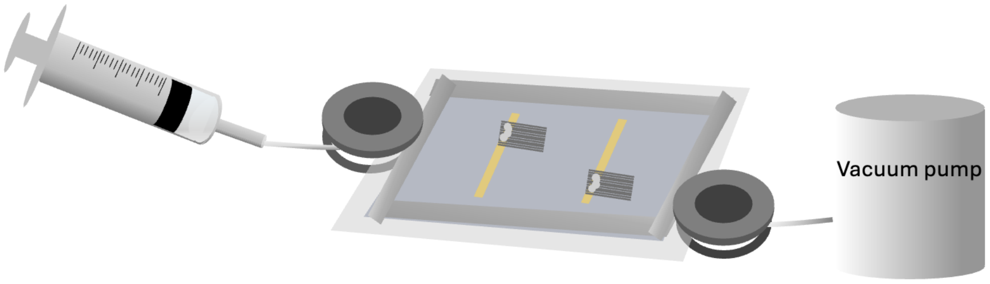

Figure 3.1: Illustration of SBE infusion.

After curing, the carbon fibres were extracted from the vacuum bag by cutting it open in an argon atmosphere. Pouch bags were then assembled with the copper foil facing the pouch material, carbon fibres placed on top, followed by a separator, lithium metal covering the fibres, and nickel foil serving as the other current collector, according to Figure 3.2. The separator was wet with small amount of liquid electrolyte. Next, the pouch bags were sealed and left for analysis.

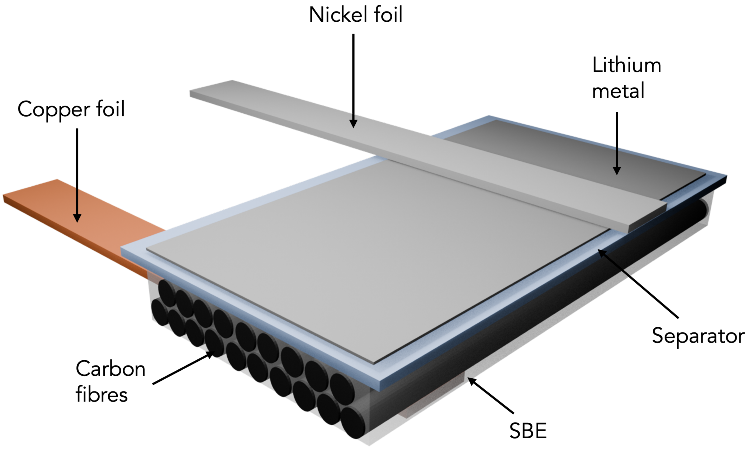

Figure 3.2: Illustration of a half-cell configuration with a negative electrode against lithium metal.

3.3 Characterisation of the structural battery electrolyte

The structural battery electrolyte was characterised using scanning electron microscopy, dynamic mechanical analysis, broadband dielectric spectroscopy to evaluate its morphology, mechanical properties, and ionic conductivity, respectively.

3.3.1 Morphology

Scanning electron microscopy (SEM) was used to investigate the morphology of the SBE. Prior to analysis, the samples were prepared for imaging by creating pieces of SBE with a cross-sectional surface, according to Figure 3.3. Some SBE was placed in a glass vial and cured for 45 minutes at 90 °C. The cured SBE was crushed, creating pieces of SBE with a cross-sectional surface. The pieces were immersed in distilled water for 24 hours to leach out the electrolyte and dried at 50 °C overnight for the liquid to evaporate. After drying, the samples were mounted onto stubs, with the cross-sectional surface facing the electron beam. To make the samples conductive, they were sputtered with gold for 1 minute, which is necessary for SEM imaging. The morphology was imaged using a scanning electron microscope (FEGSEM - Leo 1550) at an accelerating voltage of 5 kV.

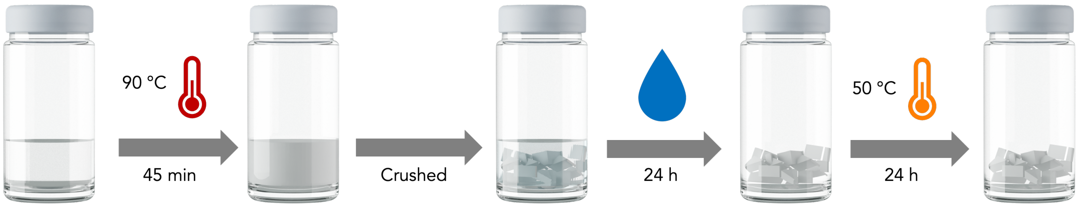

Figure 3.3: Procedure of preparing SBE samples for SEM imaging.

3.3.2 Mechanical properties

The storage modulus and the glass transition temperature (T_g) were determined using Anton Paar MCR702 rotational Rheometer for DMA measurements. The SBE solution was cured in a small syringe with a 4.6 mm diameter. The cured SBE cylinders were extracted and clamped into a holder with a 15 mm distance between the clamps. The measurements were performed in the linear viscoelastic region at a strain of 0.01% and kept isothermally at the starting temperature for 180 s prior to ramping. All measurements were performed at ω=6 rad/s. The temperature measurements were conducted in two steps, from -40 °C to 25 °C and from 25 °C to 80 °C, both at a rate of with 3 °C/min. The two datasets were combined to produce a continuous result.

3.3.3 Electrochemical properties

Broadband dielectric spectroscopy was conducted using a Novocontrol GmBH broadband dielectric spectrometer to determine the ionic conductivity of the SBE samples in a frequency range of 10^{-1} to 10^{7} Hz. A uniform sample of cured SBE with a small width (0.4-1.5 mm) was placed between two stainless-steel electrodes and screwed together to ensure full contact between the sample and the electrodes, with no air between. Temperatures were applied in 5 °C steps, from 40 °C down to -80 °C, controlled by a nitrogen gas cryostat with ± 0.5 K stability. To reduce polarization effects, an electric field of 1 V was applied.

3.4 Characterisation of half-cells

The half-cells were characterised electrochemically with three different methods. A GCD measurement was done to find the capacity, EIS was conducted to observe the resistive behaviour of the cells, and CV to ensure connection, reversibility, and stability.

3.4.1 Electrochemical testing

The finished half-cells were connected to a potentiostat for GCD testing to determine the capacity of the battery cells and observe capacity loss due to the SEI formation. The measurements were carried out between 0.01 and 1.5 V vs. Li/Li^{+} (Gamry potentiostat) at different C-rates (0.1C, 0.2C, 0.4C, 0.8C, and 0.1C) for 10 initial SEI-forming cycles, then 5 cycles at each rate, ending with 10 cycles at 0.1C. For low-temperature measurements, the same procedure was followed, except that the half-cells were put into a cooling box at approximately 10 °C. Additionally, other half-cells were put into a freezer at -15 °C for measurements. The temperature was monitored using a thermometer.

Potentiostatic EIS was performed to measure the impedance of the different half-cells, using a Gamry potentiostat. An open circuit potential (OCP) was performed for 60 seconds prior to the EIS experiment to ensure that a stable equilibrium potential was reached. The EIS measurements were carried out at a frequency range of 0.1 Hz to 20 kHz with an AC amplitude of 10 mV.

The half-cells were connected to a potentiostat (Gamry potentiostat) for CV measurements to ensure reversibility, connection, and stability. An OCP was performed for 60 seconds before measurements to ensure steady state. The half-cells were cycled three times between 0.01 and 2 V vs. Li/Li^{+} at a scan rate of 0.5 mV/s.

4

Results and discussion

The results presented are divided into four sections. Initially, the copolymer selection for the electrolyte system is discussed. The subsequent sections evaluate the electrochemical and mechanical performance of the different electrolyte systems in half-cell or SBE configurations and compare their respective properties. Lastly, the interfacial compatibility between the SBE and the carbon fibres is discussed.

4.1 Copolymer selection

DMA measurements were conducted to determine the T_g for the selection of copolymer composition (Figure 4.1). Two copolymer ratios were tested against the reference, and the measurement showed a small peak in a broad temperature range. Since the T_g could not be fully determined by the broad peaks and no major differences were observed between the different ratios, this parameter was not used a criterion for determining the copolymer ratio.

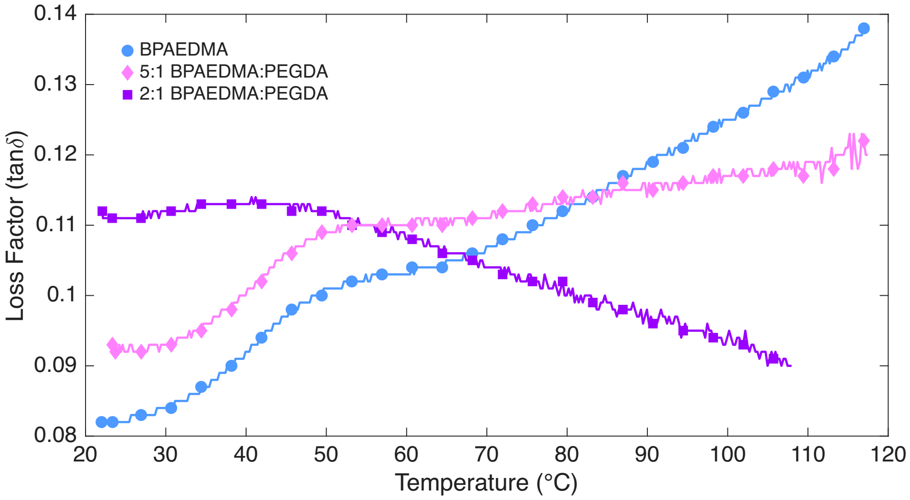

Figure 4.1: Loss factor as a function of temperature for SBE containing only BPAEDMA and copolymers 2:1 BPAEDMA:PEGDA and 5:1 BPAEDMA:PEGDA.

SEM images of the SBE bulk were taken to visualise the porosity of the different samples (Figure 4.2). Differences in porosity was observed between the samples. The 5:1 copolymer (Figure 3.3b) shows the highest porosity with larger pores than the reference sample, which is favourable for faster ionic transport. In contrast, the 2:1 copolymer (Figure 4.2a) exhibits the lowest porosity, which may hinder ion transport. Therefore, the 5:1 copolymer was chosen for further analysis.

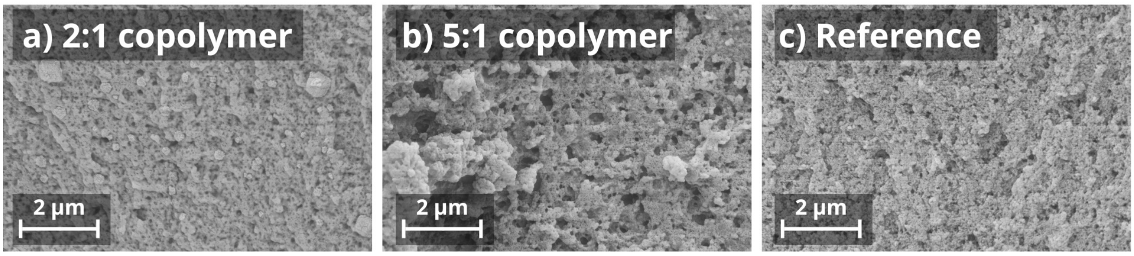

Figure 4.2: SEM images of SBEs showing copolymers a) 2:1, b) 5:1, and c) reference.

4.2 Electrochemical performance

The electrochemical performance for all compositions was evaluated in half-cell configurations. Representative voltammograms for every composition before galvanostatic cycling are shown in Figure 4.3. The peak currents increase from the first cycle to the second, while there is a minimal increase between the second and the third cycle, indicating electrode activation, stabilisation of the SEI layer, or improved wetting [35]. The peak currents for 70:30 DG:FEC are the highest (Figure 4.3b), reaching approximately 1.5 mA for the second cycle. The reference system (Figure 4.3e) exhibit similar peak currents to those of the 5:1 copolymer (Figure 4.3d). In contrast, both the 100 DG sample (Figure 4.3a) and the salt mix (Figure 4.3c) show peak currents comparable to those of the 70:30 DG:FEC system.

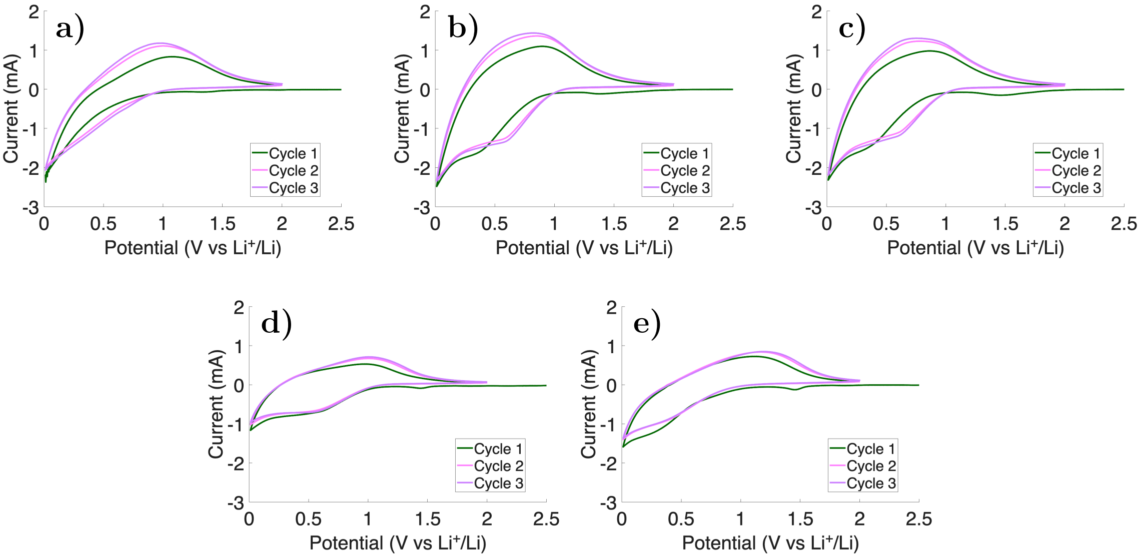

Figure 4.3: Representative cyclic voltammograms for a) 100 DG, b) 70:30 DG:FEC, c) salt mix, d) 5:1 copolymer, e) reference at scan rate 0.5 mV/s.

The high peak currents seen in Figure 4.3a-e can be explained using Randles-Ševičík equation in Equation 4.1,

$$i_p \propto A_{ea} D^{1/2} C v^{1/2} \tag{4.1}$$

where i_p is the peak current, A_{ea} the electroactive area, D the diffusion coefficient, C the concentration of active species, and v the scan rate. This indicates that a higher peak current corresponds to faster electrochemical kinetics, more electroactive area, or/and improved ion diffusion [35].

The small peak around 1.5 V in the first cycle of all voltammograms is attributed to reduction of the salt LiTFSI and, for the salt mix, LiDFOB 4.3c [36]. The broad peak seen at approximately 0.5 V for 70:30 DG:FEC in Figure 4.3b and for the salt mix in Figure 4.3c may be attributed to the reduction of FEC [37]. The reduction of the salts and solvents are contributing to the formation of the SEI layer, especially the peak at 1.5 V, which disappears after the first cycle. The broad oxidation peak is associated with the deintercalation of lithium ions [38–40]. Overall, the voltammograms display reduction peaks associated with SEI layer formation and a distinct oxidation peak, with no additional peaks indicative of side reactions.

EIS was conducted on all half-cells prior to galvanostatic cycling to evaluate their resistive behaviour. All Nyquist plots with a zoomed-in view are presented in Figure 4.4. Three half-cells were measured for each composition, except for the copolymer that has only two cells. All half-cells were measured in room temperature but were later used for cycling at -15 °C, 12 °C and 25 °C. Figure 4.4 shows minimal change in impedance between the different cells, apart from sample 70:30 DG:FEC, seen in Figure 4.4b, that shows a different resistive behaviour for two cells. However, the zoomed-in view of 70:30 DG:FEC (Figure 4.4b) shows close to identical plots with same values of solution and charge transfer resistance.

The Nyquist plots were fitted using an equivalent circuit shown in Figure 4.5 with a resistor in series with a resistor and a constant phase element (CPE) in parallel, and a CPE in series with that. The CPE describes non-ideal capacitive behaviour associated with deviations from ideal capacitor response.

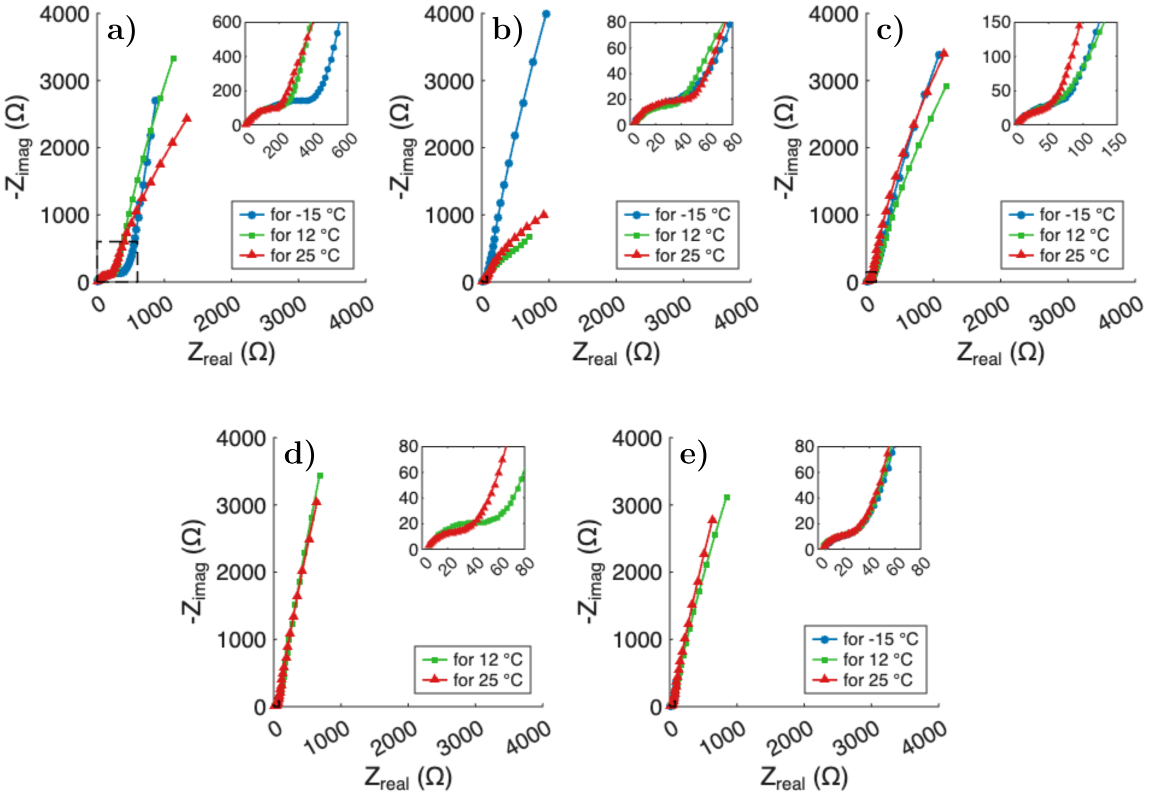

Figure 4.4: Nyquist plots with a zoomed-in view showing the variation in impedance between different cells of all compositions; a) 100 DG, b) 70:30 DG:FEC, c) salt mix, d) 5:1 copolymer, e) reference.

Semicircles are observed in all measurements, caused by the resistance in the bulk of the SBE. The observed solution resistance in all systems is between 3.5 and 7.5 Ω. The charge transfer resistance is around 30 to 100 Ω for most systems, while the 100 DG system (Figure 4.4a) exhibits higher resistance with a resistance of 300 Ω. This may be attributed to the significantly lower dielectric constant of DG (7.23 [41]), in comparison with the other solvents, where EC has a dielectric constant at 90, PC at 65 [16], and FEC at 110 [42]. A higher dielectric constant gives a stronger interaction between the solvent and the lithium ion, and a stronger solubility towards the salt. It can also be caused by different wetting abilities of the interface [16].

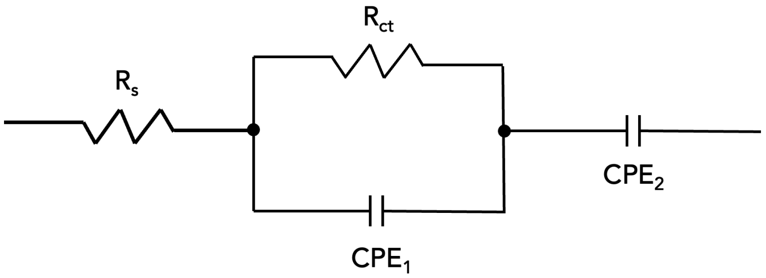

Figure 4.5: Equivalent circuit model for fitting EIS data.

The ionic conductivity of different SBEs was measured with broadband dielectric spectroscopy where all compositions showed an Arrhenius behaviour (Figure 4.6). The 100 DG and 70:30 DG:FEC samples were measured four times with the average values and standard deviation shown in Figure 4.6. The 70:30 DG:FEC sample exhibits the highest ionic conductivity over the measured temperature range.

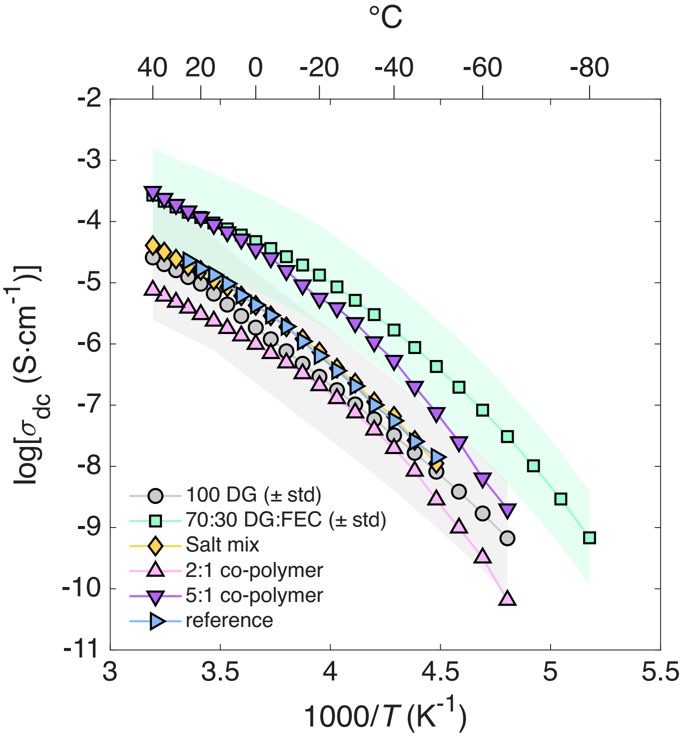

Figure 4.6: Inverse temperature dependence of ionic conductivity for different compositions of SBE.

The ionic conductivity decreases with decreasing temperature which can be attributed to sluggish ion transport due to the higher viscosity of the electrolyte [16]. The 2:1 copolymer shows the lowest ionic conductivity and likely hinders the ions to move between electrodes, which is consistent with the morphology observed in the SEM image in Figure 4.2a. The 70:30 DG:FEC and 5:1 copolymer exhibit the highest ionic conductivities, which can be attributed to their high porosity, Figure 4.7b and 4.7d. However, the 5:1 copolymer has a steeper decrease of ionic conductivity as the temperature decrease, likely due to the presence of the liquid electrolyte containing EC:PC, which exhibits poorer performance at lower temperatures.

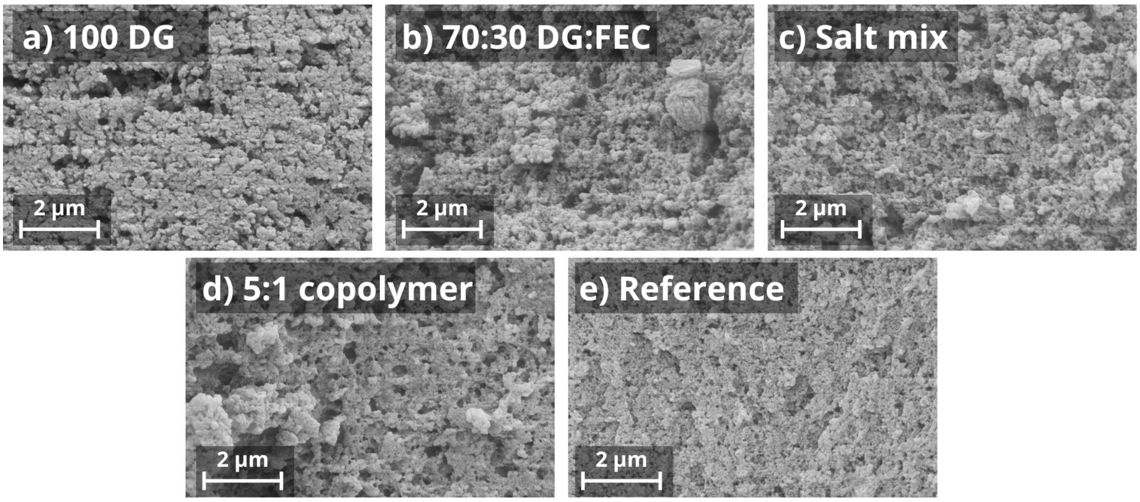

Figure 4.7: Cross-sectional SEM of different SBE compositions.

A battery must exhibit an ionic conductivity of $\sigma > 10^{-4}$ S/cm [43] to be considered as a functional battery. Conventional electrolytes have shown ionic conductivities reaching 10^{-2} S/cm, while most have an ionic conductivity around 10^{-3} S/cm [44]. The 70:30 DG:FEC shows an average ionic conductivity of 1.48 x 10^{-4} S/cm at 25 °C and decreases to 1.7 x 10^{-6} S/cm at -40 °C. The 2:1 copolymer has an ionic conductivity of 3.89 x 10^{-6} S/cm already at 25 °C. The reference system has been previously measured by Pipertzis *et al.*, showing almost one magnitude higher ionic conductivities [3]. This can be due to manufacturing differences or other experimental factors.

Galvanostatic charge-discharge cycling was conducted for all compositions at 25 °C (room temperature, RT), 12 °C (low temperature, LT), and -15 °C (freezing temperature, FT), except for the 5:1 copolymer. This was performed at the 0.1C-rate for ten consecutive cycles, followed by 5 cycles at 0.2C, 0.4C, and 0.8C, finalised by 10 cycles at 0.1C. Figure 4.8 shows the results of these measurements with the red colour representing RT, green LT, and blue FT. The specific capacity decreases with temperature and every increase of C-rate. Figure 4.8a shows the results from 100 DG where the cell cycled at 25 °C show lower specific capacity than the cell cycled at 12 °C. The specific capacity for the reference system (Figure 4.8e) is close to zero at -15 °C. The 5:1 copolymer exhibited a specific capacity under 60 mAh/g when cycled at 12 °C and was therefore not further tested at -15 °C, where similar or worse performance than the reference was anticipated.

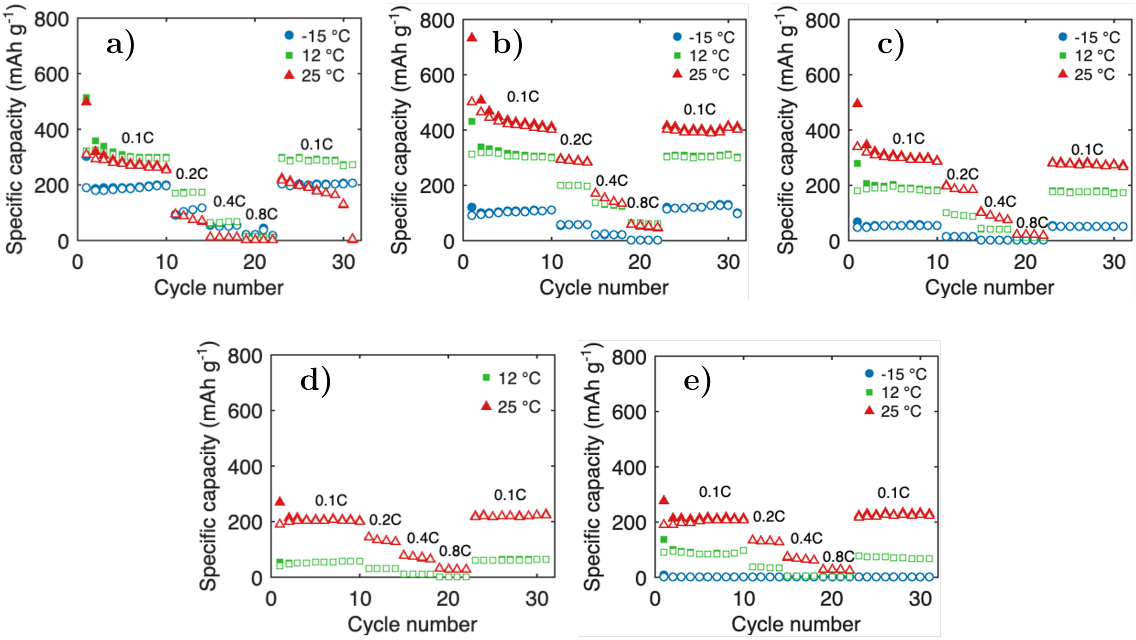

Figure 4.8: Specific capacity for each cycle number at 25 °C, 12 °C, and -15 °C for a) 100 DG, b) 70:30 DG:FEC, c) salt mix, d) 5:1 copolymer, and e) reference.

At room temperature, 70:30 DG:FEC shows an initial specific capacity of 733 mAh/g and reduces to approximately 430 mAh/g for consecutive cycles at 0.1C. This is higher than the theoretical capacity for graphite (372 mAh/g) [45]. This can be attributed to defects in the carbon fibres, miscalculations of the active mass, and/or co-intercalation. The carbon fibres are manufactured from polyacrylonitrile (PAN) precursors and contains domains of turbostratic graphite, with amorphous domains and pores that can act as defects. These defects can host lithium and therefore increase the specific capacity [46, 47]. Manipulated graphite with a holey structure has been calculated to have about 2-4.5 times higher capacities than intrinsic graphite [48]. Additionally, Ni *et al.* has shown a capacity of 526 mAh/g in the potential range of 0-2 V vs. Li/Li$^+$ using hard carbon [49]. A review by Singh *et al.* reported high specific capacities (400–500 mAh/g) for hard carbon, attributed to lithium storage via intercalation, pore filling, and adsorption on carbon surfaces [45]. Hard carbon is more disordered than carbon fibres and graphite and cannot be graphitized. The type and degree of disorder influence the capacity [50]. This suggest that the carbon fibres likely behave more as hard carbon.

The specific capacity for 100 DG at 25 °C is lower than at 12 °C and -15 °C from certain C-rates. This can be due to heating and subsequent degradation of the carbon fibres (Figure A.1 in Appendix 1), resulting in reduced electroactive area.

Comparing 100 DG and 70:30 DG:FEC (Figure 4.8a and b), 100 DG exhibits similar values of capacity as 70:30 DG:FEC at 12 °C (300 vs. 310 mAh/g), while it shows higher capacity at -15 °C (186 vs. 105 mAh/g). This may be attributed to cell issues as the GCD measurements were conducted with one cell for each temperature, limiting the reliability of the results. The EIS measurements show a higher charge transfer resistance for 100 DG compared to 70:30 DG:FEC indicating that the ion transport at the electrode/electrolyte interphase is slower for 100 DG. This should contribute to a lower capacity as ions are moving slower, charging the battery slower. However, these tests are done at 25 °C and do not explain the behaviour at -15 °C. Dielectric spectroscopy, conducted down to -80 °C show that the ion transport is faster for 70:30 DG:FEC across all temperatures, making the hypothesis of a failed cell more reliable. Additionally, the SEM images show a higher porosity for 70:30 DG:FEC than 100 DG, enabling faster ion transport.

The reference shows a specific capacity below 1 mAh/g at -15 °C which is expected as the EC:PC-based liquid electrolyte freezes around -20 °C [16]. Therefore, the same behaviour is expected for 5:1 copolymer, as it contains the same liquid electrolyte.

The high capacity of the diglyme-based systems cannot be directly translated to full cell performance. In half-cells, the potential is measured against lithium metal which acts as both a reference and a counter electrode. The lithium metal has a large specific capacity, which makes the reactions never limited to the capacity at the counter electrode. This enables access to low potentials that are difficult to reach in full cells. Although half-cells are valuable for assessing intrinsic electrochemical properties, they cannot predict the direct behaviour of a full cell. In full cells, the potential is measured between two electrodes. Commercial lithium-ion batteries have anodes with about 10% higher capacity, meaning that the capacity is limited by the cathode. As a result, half-cell capacities may be overestimated due to irreversible side reactions, SEI formation, and limited availability of cyclable lithium [51–53].

4.3 Mechanical performance

The mechanical performance was assessed between -40 °C and 80 °C for the different compositions of SBEs, with Figure 4.9a showing how the shear storage modulus is reduced with increasing temperature for all SBE compositions.

Figure 4.9b shows how the loss factor ($\tan(\delta)$) changes as a function of temperature. The loss factor is the ratio between the loss modulus and the storage modulus, where the loss modulus represents the dissipated energy during deformation, the viscous part, and the storage modulus is a measure of the energy that has been stored, the solid-like part. A lower $\tan(\delta)$ corresponds to a stiffer, more solid material and a higher number is attributed to a viscous material. Here, the values are low and increase slightly with temperature indicating a stiff and solid material that becomes more viscous with increasing temperature. There are no clear peaks indicating a phase transition. However, this is expected as the sample is a cross-linked polymer [34, 54].

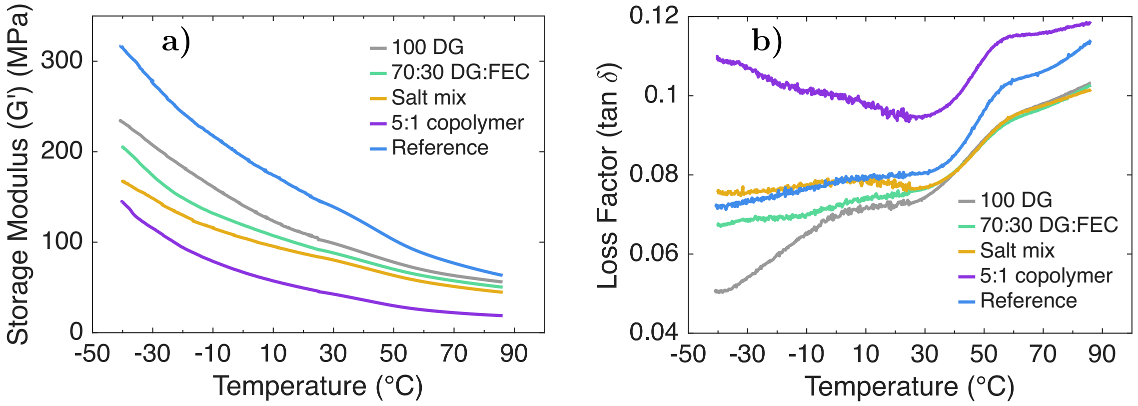

Figure 4.9: a) Storage modulus and b) the loss factor as a function of temperature for SBE samples.

To convert the observed shear storage modulus (G') to the storage modulus (E') Equation 4.2 is used with a Poisson ratio assumed to be 0.34 [55]. The measured shear storage modulus and calculated storage modulus is tabulated in Table 4.1.

$$E' = 2G'(1 + \nu) \tag{4.2}$$

Table 4.1: Shear storage modulus (G') and calculated storage modulus (E') for different SBE compositions at three different temperatures.

	-15 °C		12 °C		25 °C	
Composition	G' (MPa)	E' (MPa)	G' (MPa)	E' (MPa)	G' (MPa)	E' (MPa)
100 DG	171.8	460.5	120.7	323.5	102.7	275.2
70:30 DG:FEC	139.8	374.6	105.1	281.8	91.6	245.6
Salt mix	121.5	325.6	93.7	251.2	83.7	224.3
5:1 copolymer	86.1	230.7	55.5	148.8	45.8	122.7
Reference	229.0	613.6	170.8	457.8	145.8	390.7

The reference sample exhibits the highest shear modulus across all temperatures, with a shear storage modulus of 145.8 MPa and calculated storage modulus of 390 MPa at 25 °C, seen in Table 4.1. This is comparable to previous results reported by Abdou *et al.*, that reports a shear storage modulus of 150 MPa at room temperature for a SBE with a 1:1 ionic liquid-to-resin ratio [56]. Additionally, a storage modulus of 380 MPa was also measured for a 1:0.6 electrolyte by Ihrner *et al.* [10]. Compared to the reference, the diglyme-based compositions have lower moduli and the 5:1 copolymer exhibits the lowest modulus. The diglyme-based systems have a higher porosity than the reference, which likely contributes to their lower mechanical stiffness, as observed by SEM (Figure 4.7). The salt mix electrolyte shows the lowest storage modulus among the diglyme-based electrolytes, which may be attributed to its high porosity and possible salt aggregation, leading to localised mechanical weakness. Additionally, Figure 4.9 shows that the diglyme-based electrolytes have comparable, intermediate storage moduli. However, 100 DG exhibits the highest storage modulus among the diglyme-based systems, whereas the 5:1 copolymer shows the lowest storage modulus of all compositions. These observations are consistent with the morphology results, where a higher porosity is attributed to a lower storage modulus.

4.4 Interfacial compatibility

The compatibility between the SBE formulations and the carbon fibres was investigated by SEM analysis of the carbon fibre imprints. The SEM images shown in Figure 4.10 display the imprints of four different SBE formulations after being galvanostatic cycled at room temperature.

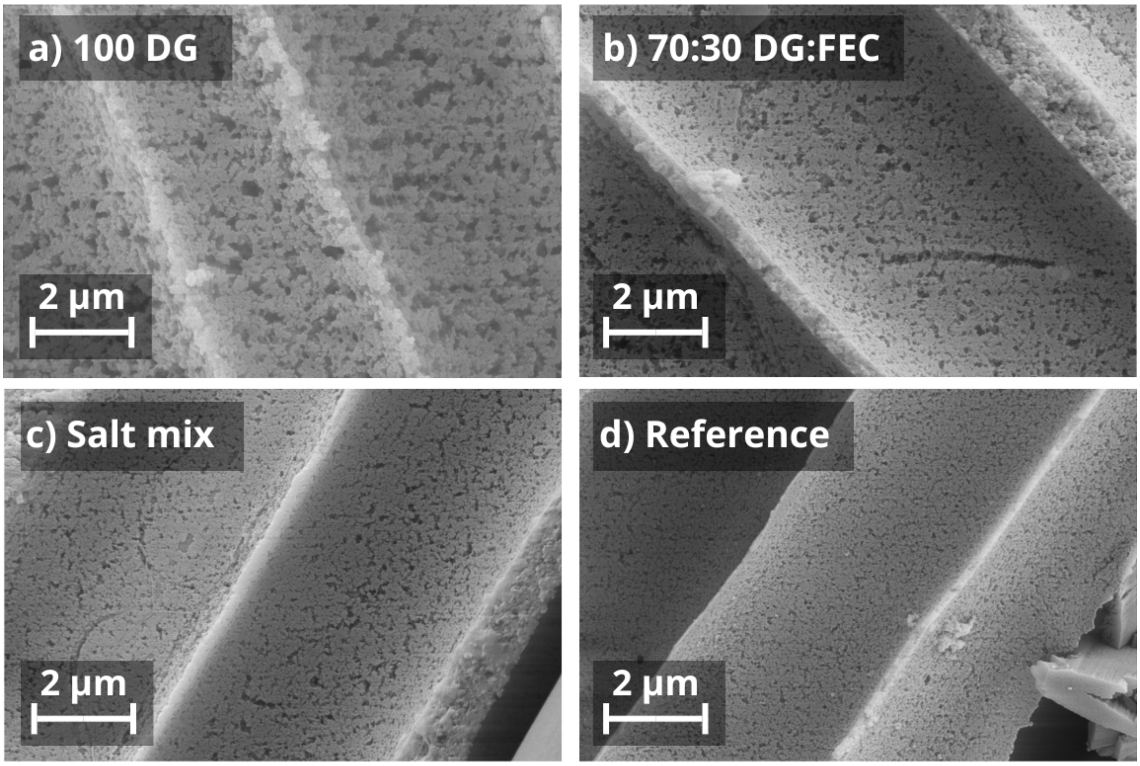

Figure 4.10: SEM images of carbon fibre imprints after cycling at room temperature for a) 100 DG, b) 70:30 DG:FEC, c) salt mix, and d) reference.

The 100 DG sample exhibits the highest porosity, with rough imprint edges. This morphology can be associated with lithium oxidation during cycling, shown by the burnt separator observed in Figure A.1 in Appendix 1. In contrast, the 70:30 DG:FEC sample displays a more homogeneous surface with well-defined imprint edges, suggesting improved contact and coverage of the carbon fibres. The salt mix also exhibits sharp edges and an intermediate porosity, similar to the 70:30 DG:FEC sample. However, both show microcracks in the surface potentially indicating localised stress during cycling. The reference has the most confined pores with sharp edges. Furthermore, all samples are intact, with no evidence of severe degradation or delamination. Overall, the imprint morphology is consistent with DMA and SEM results of the bulk samples, except for 100 DG. A higher porosity leads to a lower storage modulus, and the bulk properties stay the same after being cycled.

5

Conclusion

This thesis focused on developing and characterising new structural battery electrolytes for low-temperature operation down to -15 °C, with the aim of maintaining both electrochemical and mechanical performance. The results reveal that the diglyme-based electrolytes, especially 70:30 DG:FEC, show the most promising balance of electrochemical performance, mechanical stability, and ion transport across the studied temperature range.

Electrochemical data shows that higher porosity and a diglyme-based electrolyte contribute to a higher ionic conductivity across a wide temperature range. Highest ionic conductivity is reached for the 70:30 DG:FEC sample which exhibits an ionic conductivity reaching 1.48 x 10^{-4} S/cm at 25 °C and 1.7 x 10^{-6} S/cm at -40 °C. These trends are consistent with galvanostatic cycling behaviour which shows a decrease in specific capacity with decreasing temperature and increasing C-rate, with the 70:30 DG:FEC system giving the higher overall performance and stable specific capacities of 430 mAh/g at 25 °C and over 100 mAh/g at -15 °C at 0.1C. All diglyme-based systems show higher specific capacity than the reference system across all temperatures. The high specific capacity observed in diglyme-based systems may be attributed to carbon fibre defects and potential co-intercalation, suggesting complex charge storage mechanisms in these materials. These results are supported by morphological characterization, that confirms a stable electrolyte-electrode interface after cycling, as shown by preserved porosity observed in SEM analysis.

The mechanical performance of the samples was associated with the porosity observed in SEM images. A more confined pore structure resulted in a higher modulus, with the reference sample showing the highest storage modulus of 390 MPa at 25 °C, which further increased with decreasing temperature.

A trade-off between electrochemical and mechanical performance is observed, where more mechanically robust systems generally result in lower ionic conductivity and reduced specific capacity. These trends remain consistent at lower temperatures. However, 70:30 DG:FEC show the most promising electrolyte formulation, combining high capacity, high ionic conductivity, and mechanical stability. Furthermore, testing in full cell configurations is needed to bridge the gap between half-cell performance and real operating conditions.

6

Future work

Firstly, the electrochemical testing has shown promising capacity and ionic conductivity for the diglyme-based compositions across all investigated temperatures. In the short term, additional cells need to be manufactured and tested to confirm the reproducibility and statistical reliability of the results.

The low-temperature characterisation is limited to DMA and BDS measurements in this thesis. In the long term, this scope should be broadened to achieve a deeper understanding of the low-temperature behaviour of the system. The galvanostatic cycling should be performed under more controlled temperature conditions, including improved monitoring, and should be measured at lower temperatures than currently available. Additionally, the electrochemical testing should be extended to testing in temperatures down to -40 °C. This would be valuable for further revealing the performance limits and transport mechanisms of the system under extreme conditions.

Another key long-term priority is to further investigate the formation and evolution of SEI layer using surface-sensitive characterisation techniques, such as ToF-SIMS or XPS analysis. In particular, it would be highly beneficial to perform *in situ* or *operando* measurements during cycling to study the real-time formation and growth of the SEI layer. Such experiments would provide valuable insights into interfacial processes and structural or chemical changes within the system, thereby contributing to a more fundamental understanding and supporting future technological development. Additionally, it would be interesting to study how the SEI layer is affected by low temperatures, below 0 °C.

Finally, short-time future work could include the exploration of new electrolyte compositions, particularly different salt mixtures as well as novel copolymer formulations, in order to further optimize electrochemical performance and expand the fundamental understanding of structure to property relationships in these materials.

Bibliography

[1] S. Deshpande et al., “Low-Temperature Structural Battery Electrolytes Produced by Polymerization-Induced Phase Separation”, *ACS Applied Polymer Materials*, vol. 6, no. 11, pp. 6323–6333, Jun. 2024.

[2] R. Chaudhary, R. Tavano, J. Xu, and L. E. Asp, “Lithium-Ion Transport in Carbon Fibers for Structural Batteries”, *Advanced Energy and Sustainability Research*, vol. 7, no. 1, e202500377, Jan. 2026.

[3] A. Pipertzis, J. Xu, N. Abdou, A. Martinelli, L. E. Asp, and J. Swenson, “Ionic and electronic conductivity in structural negative electrodes”, *Electrochimica Acta*, vol. 512, p. 145 501, Feb. 2025.

[4] D. Carlstedt et al., “Multiscale modeling and calibration framework for predicting the mechanical response of Li-ion battery cell components”, *Journal of Power Sources*, vol. 659, p. 238 237, Dec. 2025.

[5] N. Nasajpour-Esfahani et al., “Comprehensive review of lithium-ion battery materials and development challenges”, *Renewable and Sustainable Energy Reviews*, vol. 203, p. 114 783, Oct. 2024.

[6] T. Jin, G. Singer, K. Liang, and Y. Yang, “Structural batteries: Advances, challenges and perspectives”, *Materials Today*, vol. 62, pp. 151–167, Jan. 2023.

[7] L. M. Schneider, A. Riazanova, D. Zenkert, and G. Lindbergh, “Effect of Electrolyte Composition on Biphasic Structural Electrolytes for Laminated Structural Batteries”, *ACS Applied Energy Materials*, vol. 7, no. 19, pp. 8838–8850, Oct. 2024.

[8] J. Eaton et al., “Model of a structural battery and its potential for system level mass savings”, *Multifunctional Materials*, vol. 2, no. 3, p. 035 002, Sep. 2019.

[9] L. E. Asp and E. S. Greenhalgh, “Structural power composites”, *Composites Science and Technology*, vol. 101, pp. 41–61, Sep. 2014.

[10] N. Ihrner, W. Johannisson, F. Sieland, D. Zenkert, and M. Johansson, “Structural lithium ion battery electrolytes via reaction induced phase-separation”, *Journal of Materials Chemistry A*, vol. 5, no. 48, pp. 25 652–25 659, Dec. 2017.

[11] M. T. Q. S. da Silva, M. do Rocio Cardoso, C. M. P. Veronese, and W. Mazer, “Tortuosity: A brief review”, *Materials Today: Proceedings*, vol. 58, pp. 1344–1349, Jan. 2022.

[12] N. Nikfarjam, P. T. Coman, C. Free, P. Ziehl, M. Sadati, and R. E. White, “Advancing ionic conductivity in solid electrolytes: Insights from polymerization-induced phase separation and microstructural optimization”, *Journal of Energy Storage*, vol. 93, p. 112 287, Jul. 2024.

[13] H. M. Boots, J. G. Kloosterboer, C. Serbutoviez, and F. J. Touwslager, “Polymerization-induced phase separation. 1. Conversion-phase diagrams”, *Macromolecules*, vol. 29, no. 24, pp. 7683–7689, Nov. 1996.

[14] G. Odian, *Principles of polymerization.* Wiley-Interscience, 2004, pp. 198–701.

[15] K. Sunil, E. Chacko, H. Mayookh Lal, A. Uthaman, and S. Thomas, “Nanostructured lithium-ion battery materials : synthesis, characterization and applications”, pp. 21–42, 2025.

[16] Y. Yang et al., “Challenges and Prospects of Low-Temperature Rechargeable Batteries: Electrolytes, Interfaces, and Electrodes”, *Advanced Science*, vol. 11, no. 46, p. 2 410 318, Dec. 2024.

[17] K. Xu, “Electrolytes and interphases in Li-ion batteries and beyond”, *Chemical Reviews*, vol. 114, no. 23, pp. 11 503–11 618, Dec. 2014.

[18] E. Peled and S. Menkin, “Review—SEI: Past, Present and Future”, *Journal of The Electrochemical Society*, vol. 164, no. 7, A1703–A1719, Jun. 2017.

[19] H. Adenusi, G. A. Chass, S. Passerini, K. V. Tian, and G. Chen, “Lithium Batteries and the Solid Electrolyte Interphase (SEI)—Progress and Outlook”, *Advanced Energy Materials*, vol. 13, no. 10, p. 2 203 307, Mar. 2023.

[20] Y. Yang, W. Yang, H. Yang, and H. Zhou, “Electrolyte design principles for low-temperature lithium-ion batteries”, *eScience*, vol. 3, no. 6, p. 100 170, Dec. 2023.

[21] National Center for Biotechnology Information, *Bisphenol A ethoxylate dimethacrylate*, 2026.

[22] Y. Fu, Y. Chen, H. Zhou, and Y. Li, “LiDFOB-based multifunctional electrolyte-enabled high cycling stability and rate capability of solid-state batteries for composite structural batteries”, *Composites Part A: Applied Science and Manufacturing*, vol. 188, p. 108 589, Jan. 2025.

[23] Y. Fu, Z. Wang, Y. Chen, X. Xu, R. Li, and Y. W. Mai, “Network-Driven Ion Transport in Robust In Situ Polymerized Electrolyte-Integrated Cathodes for Long-Life Structural Batteries in Intelligent Sensing Platforms”, *Advanced Materials*, Jan. 2025.

[24] S. Tobishima et al., “Glyme-based nonaqueous electrolytes for rechargeable lithium cells”, *Electrochimica Acta*, vol. 49, no. 6, pp. 979–987, Mar. 2004.

[25] National Center for Biothechnology Information, *Diglyme*, 2026.

[26] Z. Li, L. Wang, X. Huang, and X. He, “Lithium Bis(Trifluoromethanesulfonyl)Imide (LiTFSI): A Prominent Lithium Salt in Lithium-Ion Battery Electrolytes – Fundamentals, Progress, and Future Perspectives”, *Advanced Functional Materials*, vol. 34, no. 48, p. 2 408 319, Nov. 2024.

[27] P. Wang et al., “Dual-salt electrolyte strategy enables stable interface reaction and high-performance lithium-ion batteries at low temperature”, *Chinese Chemical Letters*, vol. 36, no. 11, p. 111 190, Nov. 2025.

[28] K. M. Krishnan, *Principles of Materials Characterization and Metrology.* Oxford University Press, 2021, pp. 693–738.

[29] A. C. Lazanas and M. I. Prodromidis, “Electrochemical Impedance SpectroscopyA Tutorial”, *ACS Measurement Science Au*, vol. 3, no. 3, pp. 162–193, Jun. 2023.

[30] *Electrochemical Impedance Spectroscopy (EIS) Basics.*

[31] N. Elgrishi, K. J. Rountree, B. D. McCarthy, E. S. Rountree, T. T. Eisenhart, and J. L. Dempsey, “A Practical Beginner’s Guide to Cyclic Voltammetry”, *Journal of Chemical Education*, vol. 95, no. 2, pp. 197–206, Feb. 2018.

[32] W. H. Woodward, “Broadband Dielectric Spectroscopy - A Practical Guide”, *ACS Symposium Series*, vol. 1375, pp. 3–59, 2021.

[33] K. Kumbhakar, T. D. Pham, K. K. Lee, K. Kwak, and M. Cho, “Dielectric relaxation spectroscopy for the characterization of ion transport in solid polymer electrolytes in Li-ion cells”, *Electrochimica Acta*, vol. 462, p. 142 759, Sep. 2023.

[34] R. Clavier, *THERMAL ANALYSIS OF POLYMERS.* John Wiley & Sons, 2008, pp. 805–840.

[35] C. H. Hamann, A. Hamnett, and W. Vielstich, *Electrochemistry.* Wiley-VCH, 2007, p. 531.

[36] J. Han, Y. Zheng, N. Guo, and P. B. Balbuena, “Calculated reduction potentials of electrolyte species in lithium Sulfur batteries”, *Journal of Physical Chemistry C*, vol. 124, no. 38, pp. 20 654–20 670, Sep. 2020.

[37] T. Hou et al., “The influence of FEC on the solvation structure and reduction reaction of LiPF6/EC electrolytes and its implication for solid electrolyte interphase formation”, *Nano Energy*, vol. 64, p. 103 881, Oct. 2019.

[38] X. Wu et al., “Effects of functional binders on electrochemical performance of graphite anode in potassium-ion batteries”, *Ionics*, vol. 25, no. 6, pp. 2563–2574, Jun. 2019.

[39] Z. Y. Wang et al., “The Regulation of Solid Electrolyte Interphase on Composite Lithium Anodes in Solid-State Batteries”, *Angewandte Chemie International Edition*, vol. 64, no. 2, e202414524, Jan. 2025.

[40] C. Shen, G. Hu, L. Z. Cheong, S. Huang, J. G. Zhang, and D. Wang, “Direct Observation of the Growth of Lithium Dendrites on Graphite Anodes by Operando EC-AFM”, *Small Methods*, vol. 2, no. 2, p. 1 700 298, Feb. 2018.

[41] K. Hoshi et al., “Purification of Perovskite Quantum Dots Using Low-Dielectric-Constant Washing Solvent "diglyme" for Highly Efficient Light-Emitting Devices”, *ACS Applied Materials and Interfaces*, vol. 10, no. 29, pp. 24 607–24 612, Jul. 2018.

[42] J. Lee et al., “Tuning Two Interfaces with Fluoroethylene Carbonate Electrolytes for High-Performance Li/LCO Batteries”, *ACS Omega*, vol. 4, no. 2, pp. 3220–3227, Feb. 2019.

[43] J. B. Goodenough and K. S. Park, “The Li-ion rechargeable battery: A perspective”, *Journal of the American Chemical Society*, vol. 135, no. 4, pp. 1167–1176, Jan. 2013.

[44] J. C. Bachman et al., “Inorganic Solid-State Electrolytes for Lithium Batteries: Mechanisms and Properties Governing Ion Conduction”, *Chemical Reviews*, vol. 116, no. 1, pp. 140–162, Jan. 2016.

[45] J. Singh, Z. Zhu, S. Han, N. Wang, and S. K. Tiwari, “Advances in hard carbon: From structural complexity to applications for next-generation technologies”, *Journal of Alloys and Compounds*, vol. 1042, p. 183 755, Oct. 2025.

[46] B. A. Newcomb, “Processing, structure, and properties of carbon fibers”, *Composites Part A: Applied Science and Manufacturing*, vol. 91, pp. 262–282, Dec. 2016.

[47] C. A. Love-Baker, T. M. Harrell, F. Vautard, J. Klett, and X. Li, “Analysis of the turbostratic structures in PAN-based carbon fibers with wide-angle x-ray diffraction”, *Carbon*, vol. 224, p. 119 037, Apr. 2024.

[48] C. Yang et al., “Holey graphite: A promising anode material with ultrahigh storage for lithium-ion battery”, *Electrochimica Acta*, vol. 346, p. 136 244, Jun. 2020.

[49] J. Ni, Y. Huang, and L. Gao, “A high-performance hard carbon for Li-ion batteries and supercapacitors application”, *Journal of Power Sources*, vol. 223, pp. 306–311, Feb. 2013.

[50] P. Kurzweil and K. Brandt, “SECONDARY BATTERIES – LITHIUM RECHARGEABLE SYSTEMS | Overview”, *Encyclopedia of Electrochemical Power Sources*, pp. 1–26, Jan. 2009.

[51] B. Rowden and N. Garcia-Araez, “Estimating lithium-ion battery behavior from half-cell data”, *Energy Reports*, vol. 7, pp. 97–103, May 2021.

[52] S. J. An, J. Li, C. Daniel, D. Mohanty, S. Nagpure, and D. L. Wood, “The state of understanding of the lithium-ion-battery graphite solid electrolyte interphase (SEI) and its relationship to formation cycling”, *Carbon*, vol. 105, pp. 52–76, Aug. 2016.

[53] F. Katzer, T. Rüther, C. Plank, F. Roth, and M. A. Danzer, “Analyses of polarisation effects and operando detection of lithium deposition in experimental half- and commercial full-cells”, *Electrochimica Acta*, vol. 436, p. 141 401, Dec. 2022.

[54] S. C. Tang and J. Pan, *Mechanics modeling of sheet metal forming.* SAE International, 2007, pp. 40–42.

[55] R. Tavano, M. Spagnol, N. Al-Ramahi, R. Joffe, J. Xu, and L. E. Asp, “Mechanical characterisation of a structural battery electrolyte”, *Polymer*, vol. 312, p. 127 646, Oct. 2024.

[56] N. Abdou et al., “Structural Battery Electrolytes Based on a Cross-Linked Methacrylate Polymer and a Protic Ionic Liquid: Is There an Optimal Composition?”, *Advanced Energy and Sustainability Research*, vol. 6, no. 5, p. 2 500 013, May 2025.

A

Appendix 1

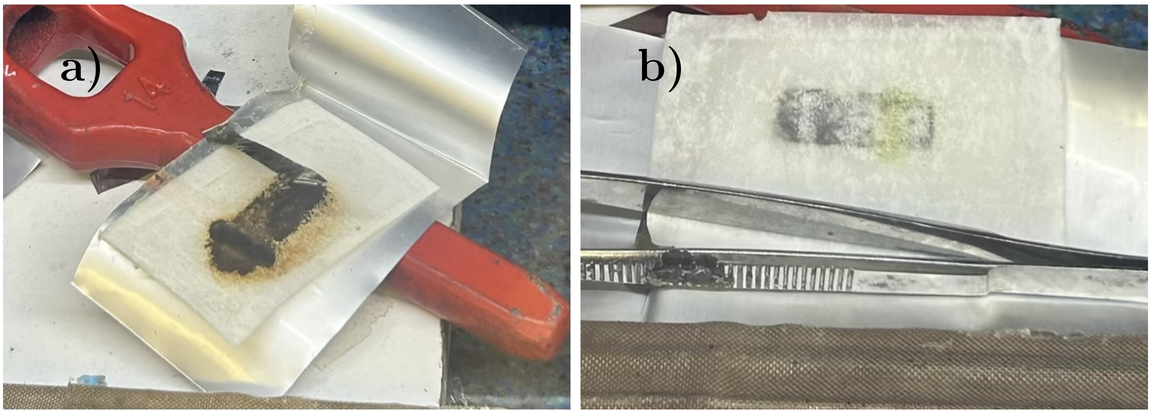

Figure A.1: Opened half-cells a) 100 DG and b) 70:30 DG:FEC.

DEPARTMENT OF SOME SUBJECT OR TECHNOLOGY
CHALMERS UNIVERSITY OF TECHNOLOGY
Gothenburg, Sweden
www.chalmers.se

`figure/auxiliary/AvancezChalmersU_black_centered-eps-conve`